Comparative studies of interatomic potentials for modeling point defects in wurtzite GaN

Huaping Lei, Jun Chen, Pierre Ruterana

Comparative studies of interatomic potentials for modeling point defects in wurtzite GaN

Huaping LEI,[1, 2, a)] Jun CHEN,[2] and Pierre RUTERANA[2]

[1)] *Key Laboratory of Materials Physics, Institute of Solid State Physics, Hefei Institutes of Physical Science, CAS, 350 Shushanhu Road, Hefei 230031, China*

[2)] *Centre de Recherche sur les Ions, les Matériaux et la Photonique (CIMAP), UMR 6252 CNRS, 6 Boulevard du Maréchal Juin, Caen 14050, France*

(Dated: 21 December 2022)

In this paper, a new version of the Stillinger-Weber (SW) potential for wurtzite GaN is presented, by which we systematically explore the structural and thermodynamical properties of native point defects and their complexes. In parallel, the semi-empirical Modified Embedded-Atom Method (MEAM) potential is selected for comparison. The SW and MEAM potentials are assessed by the reproduction of the fundamental properties of wurtzite GaN and by the ability to describe the inversion domain boundaries and the wurtzite-rocksalt phase transition. Then the structural search of native point defects and their complexes in GaN is implemented using both SW and MEAM potentials with the benchmark of Density Functional Theory (DFT) calculations. Besides vacancies and antisites, four N and five Ga interstitials are confirmed through the refining of DFT calculations, among which two N split interstitials N^+-N$\langle 2\overline{1}\overline{1}0\rangle$, N^+-Ga$\langle 01\overline{1}0\rangle$, and two Ga split interstitials Ga^+-Ga$\langle 01\overline{1}0\rangle$-g, Ga^+-N$\langle 01\overline{1}0\rangle$ are observed for the first time. The SW potential correctly predicts the octahedral occupation Ga_{Oct} to be the most stable Ga interstitial, while the MEAM potential predicts the ground state of N^+-N$\langle 01\overline{1}0\rangle$ split interstitial (N^+-N$\langle 01\overline{1}0\rangle$-g) as the most stable N interstitial. But neither of two potentials could generate simultaneously the most stable configurations of N and Ga interstitials. The investigations of point defect complexes reveal that N octahedral Frenkel ($Frenkel_{Oct}$(N)) and paired antisite ($N_{Ga}Ga_N$) defects are unstable and convert into the $V_N \oplus N^+$-N$\langle 01\overline{1}0\rangle$-g configurations with the different separations between V_N and N^+-N$\langle 01\overline{1}0\rangle$-g point defects based on the DFT calculations. The formation energies calculated by the DFT and SW potential demonstrate that Schottky, Ga octahedral Frenkel ($Frenkel_{Oct}$(Ga)) and $V_N \oplus N^+$-N$\langle 01\overline{1}0\rangle$-g point defect complexes are energetically feasible, and they should not dissociate into two isolated point defects. In contrast, the MEAM potential predicts the dissociation to be exothermic for Schottky and $V_N \oplus N^+$-N$\langle 01\overline{1}0\rangle$-g. Overall, the structural features concerned with N-N or Ga-Ga bonds relaxed by the SW potential are more consistent with DFT calculations than the MEAM counterpart.

Keywords: GaN, Point defects, empirical potentials, First-principles calculation, Molecular statics, Molecular dynamics

[a)]Corresponding author: huaping.lei@outlook.com

I. INTRODUCTION

GaN and related alloys attract scientific and industrial interests due to their unique properties[1]. They have direct band gap, high melting point, high thermal conductivity, high breakdown field, high electronic mobility and high saturation electron drift velocity. Belong to the $P6_3mc$ space group they also inherently possess spontaneous and piezoelectric polarization. In GaN the strong bonding between cation and anion atoms gives it an intrinsic thermal stability and high radiation resistance with the displacement threshold energy up to 19 eV for Ga atoms[2]. These merits make GaN-based alloys suitable for high power, high temperature and high frequency electronic devices to operate in harsh environments such as power supplies, automotive industries, aerospace communications and nuclear reactors[3–6]. However, the performance of GaN-based devices is usually restricted below the theoretical values. They suffer the permanent and/or reversible degradations due to the structural defects, which mainly consist of point defects, threading dislocations and grain boundaries *etc.*[7,8].

The point defects such as vacancies, antisites and interstitials could be generated during non-stoichiometric growth, thermal excitation[9], ion implantation[10] or irradiation damage[11,12], *etc.*. These native point defects and their complexes strongly influence the electrical and optical properties of materials. They act as traps and recombination centers for carriers[7,13] thus to deteriorate the efficiency of devices[14], and they may also impede p-type doping in GaN by inducing compensation[15]. The point defects critically control the diffusion dynamics in ion implantation, thermal annealing and recovery of irradiated damage[16]. On the other hand, they could be purposefully created to improve the performance of GaN-based devices. For instance, Ga interstitials generated in the low-fluence neutron irradiation passivate the vacancy-decorated threading dislocations thus to reduce the reverse leakage current of AlGaN/GaN heterostructures[17,18].

The atomic geometries of point defects in GaN have been identified by combining the experimental measurements[13,14,19,20] and the theoretical calculations with respect to different charge states[15,21–24]. The dominant point defect is 3+ charged N vacancy in p-type GaN[15,21–24], but it might change to 3- charged Ga vacancy in n-type GaN[15,22,23]. The atomic structures of N and Ga interstitials have been also resolved[19–22,25–27]. The N^+-N$\langle 01\bar{1}0\rangle$ configuration is recognized as the most stable N interstitial with the defect level at 1.0 eV below

the conduction band edge[19,20]. Ga interstitials are experimentally detected to possess C_{3v} symmetry[27] locating at either octahedral or tetrahedral sites, but the latter occupation is excluded afterwords since the formation energy is higher by 93 meV according to the hybrid DFT calculation[28]. In addition to the thermodynamically stable configurations, the dynamical properties of point defects have been investigated as well. The positron annihilation experiment indicates that the migration barrier of N vacancy is 2.5 eV[29] in line with the calculated value of 2.6 eV[30] (2.7 eV[31]) for 3+ charged state, while Ga vacancy migrates with a barrier of 1.5 eV[32] in agreement with the theoretical value of 1.9 eV[21,30] for 3- charged state. As for N and Ga interstitials, the minimum migration barrier is predicted to be 1.4 eV[30] (1.7 eV[31]) for 3+ charged N interstitials, and it is 0.7 eV[31] (0.9 eV[30]) for 3+ charged Ga octahedral interstitials in good agreement with the experimental value of 0.7 eV for Ga migration in the irradiated GaN[27].

Besides point defects, threading dislocations are also present in GaN due to the lattice mismatch and the different thermal expansion between epilayers and substrates. With the presence of dislocations, the long-range elastic field can drive point defects to move directionally for the release of their local strain. This causes interstitials and vacancies to migrate toward the tensile and compressive regions of dislocations, respectively. Therefore, the dislocations act as sinks for point defects to form complex defective structures analogous to the dislocation-induced phase segregation in Ga(In, Al)N alloys[33–36]. In turn, point defects influence the structural and electronic properties of threading dislocations. The vacancy-decorated a-edge dislocations form the reverse leakage current channels in AlGaN/GaN heterostructures[17,18]. Concerning the presence of external elastic field, the metastable or excited configurations of point defects are important to identify the diffusion pathways with lower migration barrier as intermediate states[19,25]. Thereby the systematical analysis of native point defects in GaN is crucial to clarify the interaction properties of point defects with threading dislocations in order to elucidate the degradation mechanisms of GaN-based devices.

The defect systems of interest contain a large amount of atoms. In order to balance reliability and efficiency, (semi-)empirical interatomic potentials are extremely suitable for the theoretical simulations. So far, several interatomic potentials have been developed for GaN, such as Stillinger-Weber (SW) potential[37,38], polymorphic Stillinger-Weber potential[39], Modified Embedded-Atom Method (MEAM) potential[40], analytical bond-order potential[41]

etc.. They have been applied to simulate the atomic structures of defects and the dynamical processes of irradiation damage. With the parameterized Ga-Ga and N-N interactions[37], the SW potential was used to investigate threading dislocations[38,42,43], partial dislocations[44], tilt grain boundaries[45,46] and point defect[26] *etc.*. However, the version of SW potential[38] used in the literature[26] fails to reproduce the most stable configurations of N and Ga interstitials. Considering the successful applications in the studies of defective structures, it is worth optimizing the SW potential continually to improve its performance in the simulation of point defects. As an alternative option, the MEAM potential for GaN developed by Do *et al.*[40] could additionally describe the elemental states of Ga and N atoms so that it is inherently applicable to simulate the growth process involving the dissolution or association of N_2 molecule and the clustering of Ga atoms. However, the assessment of MEAM potential is still lacking to describe point defects or threading dislocations in wurtzite GaN. On the other hand, the atomic structures of native point defects in GaN have not been completely searched out yet as presented in the next sections.

Therefore, the purpose of this work is two folds. (1) To further modify the SW potential for GaN and perform the assessments of it in comparison with the MEAM counterpart. (2) To systematically explore the native point defects and their complexes in GaN using both potentials. Subsequently, the structural and thermodynamical properties of defective structures are refined by DFT calculations, which thus serves as the assessment of two potentials in the simulation of systems containing point defects. Accordingly, in Sec. II, the formalism of SW potential is described in brief with the presence of the corresponding parameters for Ga-N, Ga-Ga and N-N interactions in triplet format. The default computational details are introduced here, and the exceptions will be stated whenever they are implemented. In Sec. III, the fundamental properties of wurtzite GaN including the lattice parameters, elastic constants and phonon dispersion are reproduced by the SW and MEAM potentials followed by their assessments of inversion domain boundaries and multiple crystallographic structures. Sec. IV presents the systematical exploration of the native point defects and their complexes using the two potentials with the benchmark of DFT calculations, the atomic structures and the thermal stability of which are discussed in details. Finally, the summaries are given in Sec. V.

II. POTENTIAL MODEL AND COMPUTATIONAL DETAILS

A. Formalism of Stillinger-Weber potential

In the Stillinger-Weber potential[47] the total energy E of N-atom system is truncated to the two-body ϕ_2 and three-body ϕ_3 terms restricted to the second nearest neighbors:

$$E(\boldsymbol{r}_1, \boldsymbol{r}_2, \cdots, \boldsymbol{r}_N) = \sum_{\substack{i,j \\ (i<j)}}^{N} \phi_2(\boldsymbol{r}_i, \boldsymbol{r}_j) + \sum_{\substack{i,j,k \\ (i\neq j; j<k)}}^{N} \phi_3(\boldsymbol{r}_i, \boldsymbol{r}_j, \boldsymbol{r}_k),$$

where

$$\phi_2(\boldsymbol{r}_i, \boldsymbol{r}_j) = A\epsilon \left[B(\frac{r_{ij}}{\sigma})^{-p} - (\frac{r_{ij}}{\sigma})^{-q} \right] \exp\left(\frac{1}{r_{ij}/\sigma - a} \right), \tag{1}$$

$$\phi_3(\boldsymbol{r}_i, \boldsymbol{r}_j, \boldsymbol{r}_k) = \lambda\epsilon(\cos\theta_{jik} + 1/3)^2 \exp\left(\frac{\gamma}{r_{ij}/\sigma - a} \right) \exp\left(\frac{\gamma}{r_{ik}/\sigma - a} \right). \tag{2}$$

Here r_{ij} is the distance between i, j atoms. ϵ and σ are the energy and distance scales, respectively. a represents the cut-off distance in which the interatomic interactions are counted. θ_{jik} is the angle between $\boldsymbol{r}_{ji}$ and $\boldsymbol{r}_{ik}$ bond vectors subtended at the vertex i atom. A, B, λ and γ are the corresponding bond strength factors.

Besides the regular terms of N-Ga-Ga (Ga-N-N), N-N-N and Ga-Ga-Ga, the N-Ga-N (N-N-Ga) and Ga-Ga-N (Ga-N-Ga) triplets are *explicitly* considered and optimized in the current version of SW potential. In the beginning, the parameters of the four regular triplets take the values presented by Béré *et al.*[38], the geometric mean of which is assigned to the other four triplets as the initial values. The parameters $\gamma = 1.2$, $p = 4$ and $q = 0$ are preserved as usual[37,38]. Then the other potential parameters are further modified[48] so that the lattice parameters, elastic constants of wurtzite GaN as well as the atomic geometries and the formation energy of two inversion domain boundaries (Holt[49] and Star types[50]) are reproduced as well as possible. The optimized results will be presented with other assessments in Sec. III. In the optimization procedure, the energy scale ϵ is reassigned by the one-fourth of cohesive energy (-9.058 eV) of GaN[51] for N-Ga bonds, the bond energy (1.731 eV) of N-N single bond[52] for N-N bonds, and the half of cohesive energy (-2.810 eV) of Ga metals[53] for Ga-Ga bonds, respectively. Finally, the whole set of potential parameters are presented in Table I for GaN.

B. Computational details

In this paper, all Molecular Statics (MS) and Molecular Dynamics (MD) simulations based on the SW and MEAM potentials are carried out by Large-scale Atomic/Molecular Massively Parallel Simulator (LAMMPS) package[54]. By default, the energy and force tolerance is respectively set to 10^{-15} eV and 10^{-12} eV/Å for the structural relaxation in MS simulation. The Density Functional Theory (DFT) calculations are implemented using Vienna Ab initio Simulation Package (VASP) code[55]. The electron-ionic interaction is described by the Projector Augmented Wave (PAW) method[56], where $2s^2$, $2p^3$ electrons of nitrogen and $3d^{10}$, $4s^2$ and $4p^1$ electrons of gallium atoms are taken as the valence states, respectively. The Perdew-Burke-Ernzerhof (PBE) scheme[57] is used for the exchange and correlation functional. The energy tolerance is 10^{-6} eV in the electronic iteration and the force is minimized to 0.01 eV/Å during the geometry optimization. The conjugate gradient algorithm and the periodic boundary condition are applied in the calculations of empirical potential and DFT method. The geometries of supercells and the atomic positions are relaxed fully.

III. ASSESSMENT OF EMPIRICAL POTENTIALS

A. Lattice parameters

The primitive cell of wurtzite GaN is illustrated in Fig. 1. As seen in Table II, both the SW and MEAM potentials reasonably reproduce the lattice constants a and c of wurtzite GaN. But the ratio of c/a and the internal structural parameter u deviate from the experimental values[58] due to the lack of long range interactions over the third-nearest neighbors in the two empirical potentials, such as electrostatic effect.

B. Elastic properties

The elastic parameters are calculated by the SW and MEAM potentials in comparison with the Antenna-Transmission Acoustic-Resonance (ATAR) experimental data[59] as presented in Table II. The elastic constants are directly calculated according to their definition $C_{ij} = \partial \boldsymbol{F}_i / \partial \boldsymbol{x}_j$, where $\boldsymbol{F}_i$ is the force along $\boldsymbol{x}_i$ axis on the $\boldsymbol{x}_j$ plane. For the wurtzite phase of GaN, there are five independent elastic constants[9] as $C_{11} = C_{22}$, C_{33}, $C_{12} = C_{21}$,

$C_{13} = C_{31} = C_{23} = C_{32}$, $C_{44} = C_{55}$, and $C_{66} = (C_{11} - C_{12})/2$. The bulk modulus is calculated as $B = \frac{C_{33}(C_{11}+C_{12})-2(C_{13})^2}{C_{11}+C_{12}+2C_{33}-4C_{13}}$. The maximum deviation from the experimental data is 8.8% (C_{13}) for the SW potential but 14.0% (C_{12}) high for the MEAM counterpart. The elastic constants and bulk modulus calculated by the SW potential are also in good agreement with DFT calculations[40]. Therefore, the SW potential presented in Table I can properly describe the mechanical properties of GaN.

C. Phonon dispersion

The phonon dispersion characterizes the collective vibration of atoms around their equilibrium lattice positions with respect to the wave vectors. The branches of phonon dispersion reflect the specific features of crystal structure and the interatomic interaction[60]. In order to investigate the thermal properties of GaN and the dynamical properties of lattice defects correspondingly, it is necessary to assess the performance of empirical potentials to reproduce the phonon dispersion of crystals.

The phonon dispersion of GaN is calculated using the FixPhonon module[61,62] in LAMMPS. In this method, the elements of dynamical matrix are constructed directly from the long-time trajectories of atoms in the MD simulations, since the ensemble average of the second moment of atomic displacements at a finite temperature is equal to the lattice Green's function coefficient, which is inversely proportional to the force constant according to the fluctuation-dissipation theorem[63].

Since GaN is stiff with the high elastic constants as shown in Table II, a large supercell is critically required for the computational convergence of dynamical matrices, the size of which is optimized to be $14a \times 14a \times 12c$[64] along the $[2\overline{1}\overline{1}0]$, $[\overline{1}2\overline{1}0]$ and $[0001]$ directions, respectively. Totally 9408 atoms are contained. The MD simulations are implemented in the microcanonical ensemble with the Langevin thermostat[65], in which the damp parameter is 0.2, and the time step is set to 2 fs. The system pressure is adjusted to 1 atmosphere with the temperature of 0.1 K. The atomic displacements are recorded for 20 ns after the time of 1 ns for the thermal equilibration of system. The phonon dispersion and the Phonon Density Of States (PDOS) are subsequently calculated using the auxiliary post-processing code *phana*[62] and shown in Fig. 2 for the SW and MEAM potentials. The phonon frequencies at some high-symmetry k points in Brillouin zone are listed in Table III in comparison with the

experimental data of Inelastic X-Ray Scattering (IXS) at 300 K[66] and of Raman scattering at 6K[67]. The results of density-functional perturbation theory (DFPT) calculations[66] are also listed for comparison.

As shown in Fig. 2, both SW and MEAM potentials yield twelve phonon dispersion branches for the 4-atom primitive cell of wurtzite GaN (Fig. 1). In the acoustic regime, the curve profile, energy spanning and symmetry degeneracies of the longitudinal-acoustic (LA) and transverse-acoustic (TA) branches are consistent with DFPT calculation (Fig. 2 in Reference[66]) very well, but agree fairly for the profile of longitudinal-optical (LO) and transverse-optical (TO) branches in the high energy regime. Specially along the Γ-A direction, the energy interval between LO and TO phonon calculated by two empirical potentials is much smaller than that of DFPT calculation. Typically, at A point the frequency interval is estimated to be 5.3 THz in DFPT calculation[66], while it is only about 0.6 THz for the SW and MEAM potentials. The deviation of the optical phonon branches could originate from the lack of long range electrostatic interaction in the used empirical potentials, which is characteristic in polar materials and results in the LO-TO splitting[68]. In details, when the wave vector is along the Γ-A direction, the spontaneous polarization contributes to the interatomic interaction parallel to the $\boldsymbol{c}$ axis more than the components within the $\boldsymbol{c}$ plane. In this regard, the extra polarization effect causes an additional force for the longitudinal mode in comparison to the transverse mode for the atomic vibration within Ga-N pairs, which yields higher frequency for LO phonon than TO phonon. In addition, the phonon frequencies calculated by the SW and MEAM potentials are broadly higher than either the experimental data or DFPT calculations throughout the entire Brillouin zone as indicated in Table III. Taking the results of DFPT calculation[66] as reference, the maximum deviation happens along three TO modes (A1(TO), E1(TO) and E2) at Γ point, which is up to 7.5 THz (31 meV) and 8.5 THz (35 meV) for the SW and MEAM potentials, respectively. The values are rather smaller than the energy scale interested in the following investigation of point defects, and the SW and MEAM potentials are thus reasonably acceptable to describe interatomic interactions in GaN.

D. Inversion domain boundaries

Besides the regular Ga-N bonds, the interactions of Ga-Ga and N-N pairs are considered in the SW and MEAM potentials as well. A typical planar defect of Inversion Domain Boundary (IDB) is selected for the optimization and assessment of the corresponding potential parameters. The IDB structures have two atomic configurations. One is the Holt-type denoted as IDB^{H}[49], where Ga and N atoms are interchanged to occupy the opponent sites in their sublattice to form a boundary along the $\{01\bar{1}0\}$ plane as shown in Fig. 3 (Left). The generated Ga-Ga and N-N bonds are alternately arranged along the boundary of IDB^{H}. The other configuration of IDB is denoted as IDB^{*}[50,69,70], which is formed by translating one side of IDB^{H} by $c/2$ along the [0001] direction to avoid Ga-Ga and N-N bonds. Then 4-fold and 8-fold atomic rings are formed in pair along the boundary as shown in Fig. 3 (Right).

In order to preserve the periodicity, two same IDB boundaries are introduced into one supercell, which are arranged reversely with the same interval along the $[01\bar{1}0]$ direction. The size of supercell is taken as $8\sqrt{3}a \times 1c \times 2a$ along the $[01\bar{1}0]$, [0001] and $[2\bar{1}\bar{1}0]$ directions, respectively. 128 atoms are contained inside. The formation energy E_{form} of IDB structures is defined as $E_{\text{form}} = (E_{\text{IDB}} - E_0)/2S$, where E_{IDB} and E_0 are the total energy of the defective and perfect structures, respectively. S is the area of the single interface. The relaxed bond length of N-N and Ga-Ga bonds in IDB^{H} and the averaged bond length of N-Ga bonds in 4-fold atomic rings of IDB^{*} are presented in Table IV in comparison with DFT calculations[50].

The formation energies of IDB^{*} and IDB^{H} calculated by the SW and MEAM potentials indicate that IDB^{H} is less stable than IDB^{*} configuration in agreement with DFT calculations[50]. The value of formation energy of IDB^{*} calculated by the MEAM potential is closer to the result of DFT calculation than the SW potential. But the atomic geometries of two IDB structures relaxed by the SW potential are more consistent with DFT calculations as indicated by the more similar N-N and Ga-Ga bond length in IDB^{H} and by the identically rectangular shape of 4-fold atomic ring in IDB^{*} structure (Fig. 1 (b) in Reference[50]), respectively. The MEAM potential generates shorter N-N and Ga-Ga bonds in IDB^{H} and a tilted shape of 4-fold atomic ring in IDB^{*} structures. The shorter N-N and Ga-Ga bonds in IDB^{H} could be attributed to the shorter equilibrium distance (1.10 Å) and higher cohesive energy (4.88 eV) of N-N dimer in the MEAM potential[71]. In the relaxation of IDB^{H} structure, the N-N and Ga-Ga bonds competitively deform to minimize the system

energy, which expands N-N but compresses Ga-Ga bonds, and the distortion is dominantly suffered by Ga-Ga bonds. However, the equilibrium distance of N-N and Ga-Ga bonds is respectively 1.47 Å and 2.39 Å in the SW potential, close to the N-Ga bond length of 1.95 Å. Accordingly, the interface of IDB^H structure is distorted fairly when using the SW potential. The tilted 4-fold atomic rings in IDB^* structure could be also ascribed to the parameters of MEAM potential, in which the minimum screening cutoff C_{min} is 2.0 for N-N pairs and 1.4 for Ga-Ga pairs[40]. Beginning with the rectangular 4-fold atomic rings, more atoms (either Ga or N atoms) will be involved into the screening effect when the diagonal N-N interaction is accounted than the case of Ga-Ga interaction, so that the N-N bonds are weakened much more than the diagonal Ga-Ga bonds to cause the shear deformation during the structural relaxation.

Therefore, the SW and MEAM potentials are applicable to the defective structures containing N-N and Ga-Ga bonds besides the regular N-Ga ones. The former would be good at the structural description while the latter would be more precise to the energy calculation.

E. Multiple crystallographic structures

In order to evaluate the transferability of the SW and MEAM potentials with respect to different atomic environments, the wurtzite, zinc-blende and rocksalt structures with different coordinate numbers are considered. In the wurtzite and zinc-blende phases, each cation (anion) has 4 neighboring anions (cations) in a tetrahedral coordination, whereas in the rocksalt phase, each cation (anion) binds 6 neighboring anions (cations) to form an octahedral structure. The binding energies as function of volume per formula unit (N-Ga) in the three lattices are plotted in Fig. 4. The wurtzite and zinc-blende phases can not be distinguished by either SW or MEAM potentials since the cutoff radius is restricted to the second nearest neighbors in GaN. Nevertheless, the wurtzite and zinc-blende phases are more stable than rocksalt in agreement with the experiment[72] and DFT calculation[73]. Moreover, the rocksalt phase is stable under high pressure. The equilibrium transition pressure P_{T} for the wurtzite-rocksalt phase transition is 52.2 GPa in experiment[72] and 44.5 GPa as predicted by DFT calculation[73]. P_{T} could be estimated by the common tangent construction of two energy curves in Fig. 4. Obviously, *only* the MEAM potential could qualitatively describe the wurtzite-rocksalt phase transition even the calculated value of P_{T} is fairly high (106

GPa). The SW potential fails to predict the phase transition since the three-body term is rigid to fix the tetrahedral configuration determined by sp^3 hybridization. Indeed, any distortion from the ideal structure increases the system energy, so the energy curves of wurtzite and rocksalt phases can not cross within a reasonable strain range and no sound value could be estimated for P_{T}.

Therefore, the MEAM potential is more transferable to treat the structural change in regard to the variation of coordinate numbers, but the SW potential is still applicable to describe the atomic structures not far away from the tetrahedral type.

IV. EXPLORATION OF NATIVE POINT DEFECTS AND THEIR COMPLEXES

A. Native point defects

With the SW potential parameterized in Table I, we explore the atomic structures of point defects in wurtzite GaN in comparison with the calculations based on the MEAM potential. The configurations of native point defects include three types, namely vacancy, antisite and interstitial. We first investigate the single point defects and then the point defect complexes made up of two point defects.

The native point defects and their complexes are modeled using a supercell with the size of $5a \times 3\sqrt{3}a \times 3c$ along the $[2\overline{1}\overline{1}0]$, $[01\overline{1}0]$ and [0001] direction, respectively. 360 atoms are contained for the perfect structure. As illustrated in Fig. 5, the possible atomic structures of native point defects are constructed as follows, and the split interstitials are denoted according to the orientation of dumbbells: (1) Anion (Cation) vacancies, $\mathrm{V_N}$ ($\mathrm{V_{Ga}}$), where a N (Ga) atom is removed from GaN bulk. (2) Anion (Cation) antisites, $\mathrm{N_{Ga}}$ ($\mathrm{Ga_N}$), where the host Ga (N) atom is replaced by a N (Ga) atom. (3) Anion (Cation) octahedral/tetrahedral interstitials, $\mathrm{N_{Oct}}$ ($\mathrm{Ga_{Oct}}$)/$\mathrm{N_{Tet}}$ ($\mathrm{Ga_{Tet}}$), where a N (Ga) atom occupies the octahedral/tetrahedral site in the shuffle plane as labeled in Fig. 1 (b). (4) $\langle 2\overline{1}\overline{1}0\rangle$-oriented split interstitials, $\mathrm{N^+}$-N$\langle 2\overline{1}\overline{1}0\rangle$ ($\mathrm{Ga^+}$-N$\langle 2\overline{1}\overline{1}0\rangle$) and $\mathrm{N^+}$-Ga$\langle 2\overline{1}\overline{1}0\rangle$ ($\mathrm{Ga^+}$-Ga$\langle 2\overline{1}\overline{1}0\rangle$), where one N (Ga) interstitial (labeled by the symbol of '+' on the right superscript) and a host N or Ga atom share the same lattice position to form a dumbbell with the axis along the $\langle 2\overline{1}\overline{1}0\rangle$ direction in the glide plane as labeled in Fig. 1 (b). Similarly, (5) $\langle 01\overline{1}0\rangle$-oriented split interstitials,

N^+-N$\langle 01\bar{1}0\rangle$ (Ga^+-N$\langle 01\bar{1}0\rangle$) and N^+-Ga$\langle 01\bar{1}0\rangle$ (Ga^+-Ga$\langle 01\bar{1}0\rangle$), where one N (Ga) interstitial and a host N or Ga atom share the same lattice position to form a dumbbell with the axis along the $\langle 01\bar{1}0\rangle$ direction in the glide plane. Due to the lack of mirror symmetry about the $\{01\bar{1}0\}$ plane, the polarized N-Ga dumbbells are not equivalent when they orientate along the $\langle 01\bar{1}0\rangle$ and its *opposite* directions, so the other two configurations are constructed by reversing the direction of N-Ga dumbbells, which are denoted as Ga^+-N$\langle 01\bar{1}0\rangle$-o and N^+-Ga$\langle 01\bar{1}0\rangle$-o, respectively. Totally eighteen different candidates are built as the initial atomic configurations. The defective structures are relaxed by the SW and MEAM potentials. Some of initial configurations convert into the identical atomic structures after the structural relaxation. The obtained atomic structures are further refined by the relaxation of DFT calculations. The computational details have been presented in Sec. II B.

The atomic structures relaxed by the SW, MEAM potentials and DFT calculations are shown in Figs. 6, 7 and 8, respectively. The atomic configurations of V_N, V_{Ga} and Ga_N are preserved after the structural relaxation of three methods despite the observable deformation of Ga-Ga bonds in Ga_N, which are expanded by +15.6%, +11.8% and +17.9% in average over the ideal N-Ga bonds in the relaxation of SW, MEAM potentials and DFT calculation, respectively. As for N_{Ga} antisite, the atomic configuration is preserved in the relaxation of SW potential (Fig. 6 (c)), while the N atom shifts upward to occupy the tetrahedral site when the MEAM potential is applied as shown in Fig. 7 (c). Close to the result of SW potential, Fig. 8 (c) indicates that the N atom of the DFT-relaxed N_{Ga} antisite shifts aside slightly to form a N^+-N$\langle 01\bar{1}0\rangle$ dumbbell in the glide space instead of the reported N^+-N$\langle 0001\rangle$ split interstitial[26]. The N-N bond length is 1.24 Å in the formed N-N dumbbell.

The initial configurations of N interstitials illustrated in Fig. 5 are not all preserved in the structural relaxations of three methods. Based on the calculations of SW potential, N^+-N$\langle 01\bar{1}0\rangle$-g, N^+-N$\langle 2\bar{1}\bar{1}0\rangle$ and N^+-N$\langle 01\bar{1}0\rangle$-e split interstitials are obtained as shown in Figs. 6 (e), (f) and (g), respectively. N^+-N$\langle 01\bar{1}0\rangle$-g and N^+-N$\langle 01\bar{1}0\rangle$-e denote the ground and excited states of N^+-N$\langle 01\bar{1}0\rangle$ split interstitials as proposed in Reference[19]. N^+-N$\langle 01\bar{1}0\rangle$-g split interstitial is relaxed from N_{Tet} and N^+-Ga$\langle 2\bar{1}\bar{1}0\rangle$ initial configurations, while N^+-N$\langle 01\bar{1}0\rangle$-e is relaxed from N^+-N$\langle 01\bar{1}0\rangle$ and N^+-Ga$\langle 01\bar{1}0\rangle$-o ones. In N^+-N$\langle 01\bar{1}0\rangle$-g split interstitial, the N-N dumbbell is almost parallel to the $\{03\bar{3}4\}$ plane (Refer to the inset of Fig. 8.), whereas the N-N dumbbell turns to be nearly perpendicular to the $\langle 03\bar{3}4\rangle$ plane and forms a small tetrahedron with two neighboring Ga atoms in N^+-N$\langle 01\bar{1}0\rangle$-e split

interstitial. The bond length of N-N dumbbell is of 1.35 Å in N^+-N$\langle 01\bar{1}0\rangle$-g, 1.45 Å in N^+-N$\langle 2\bar{1}\bar{1}0\rangle$ and 1.35 Å in N^+-N$\langle 01\bar{1}0\rangle$-e split interstitials, respectively, all of which considerably agree with the values relaxed in the following DFT calculations. As shown in Fig. 6 (h), the configuration of N_{Oct} interstitial is preserved in the relaxation of SW potential, and N^+-Ga$\langle 01\bar{1}0\rangle$ split interstitial is unstable and convert into N_{Oct} as well, which is different from the relaxations of MEAM potential and DFT calculations.

Besides four N interstitials (N^+-N$\langle 01\bar{1}0\rangle$-g, N^+-N$\langle 2\bar{1}\bar{1}0\rangle$, N^+-N$\langle 01\bar{1}0\rangle$-e and N_{Oct}) in common with the results of SW potential, the MEAM potential additionally predicts N tetrahedral interstitial N_{Tet} and N^+-Ga$\langle 01\bar{1}0\rangle$ split interstitial, all of which are shown in Figs. 7 (e)-(j). After the structural relaxations of MEAM potential, N^+-N$\langle 01\bar{1}0\rangle$ and N^+-Ga$\langle 2\bar{1}\bar{1}0\rangle$ initial configurations convert into N^+-N$\langle 01\bar{1}0\rangle$-g split interstitial, while N^+-N$\langle 01\bar{1}0\rangle$-e split interstitial is relaxed from N^+-Ga$\langle 01\bar{1}0\rangle$-o initial configuration. It should be stressed that in N^+-N$\langle 01\bar{1}0\rangle$-g split interstitial relaxed by the MEAM potential, the N-N dumbbell is instead almost parallel to the $\{0\bar{3}38\}$ plane (Refer to the inset of Fig. 8.) as seen in Fig. 7 (e), which is different from the results of SW potential and the latter DFT calculation. In N_{Tet} interstitial, the N atom occupied the tetrahedral site binds with the host N and Ga atoms to form a straight Ga-N-N-Ga atomic chain along the [0001] direction as shown in Fig. 7 (j). The bond length of N-N dumbbell is of 1.11 Å in N^+-N$\langle 01\bar{1}0\rangle$-g, 2.29 Å in N^+-N$\langle 2\bar{1}\bar{1}0\rangle$, 1.13 Å in N^+-N$\langle 01\bar{1}0\rangle$-e split interstitials and 1.10 Å in N_{Tet}, respectively. The N-Ga dumbbell in N^+-Ga$\langle 01\bar{1}0\rangle$ split interstitial is in tensile state with the bond length of 1.96 Å longer than the ideal value of 1.94 Å for N-Ga bonds in the perfect structure.

After the refinement of DFT calculations, N^+-N$\langle 01\bar{1}0\rangle$-g, N^+-N$\langle 2\bar{1}\bar{1}0\rangle$, N^+-N$\langle 01\bar{1}0\rangle$-e and N^+-Ga$\langle 01\bar{1}0\rangle$ four N split interstitials are obtained as shown in Figs. 8 (e)-(h). N_{Oct} and N_{Tet} interstitials are unstable and convert into N^+-N$\langle 01\bar{1}0\rangle$-g split interstitial. Nevertheless, the structural stability of N_{Oct} is still in doubt even on the same level of the first-principles calculations. For instance, it has been produced when the hybrid quantum mechanical/molecular mechanical (QM/MM) approach is applied with either B97-2 or BB1k exchange-correlation functionals[23]. The corresponding discussion with respect to the different computational schemes is beyond the scope of this work thus to be omitted here. Similar to the result of SW potential (Fig. 6 (e)), the N-N dumbbell in the DFT-relaxed N^+-N$\langle 01\bar{1}0\rangle$-g split interstitial is nearly parallel to the $\{03\bar{3}4\}$ plane as shown in Fig. 8 (e), and each N atom of N-N dumbbell binds two neighboring Ga atoms. The bond length of N-N dumbbell is

of 1.35 Å in agreement with the reported value[25]. In the DFT-relaxed N^+-N$\langle 01\bar{1}0\rangle$-e split interstitial (Fig. 8 (g)), the N-N dumbbell is almost perpendicular to the $\{03\bar{3}4\}$ plane to form a small tetrahedron with two neighboring Ga atoms as well, the bond length of which is 1.37 Å. Besides two N^+-N$\langle 01\bar{1}0\rangle$ split interstitials, N^+-N$\langle 2\bar{1}\bar{1}0\rangle$ and N^+-Ga$\langle 01\bar{1}0\rangle$ configurations are newly explored in this study. In N^+-N$\langle 2\bar{1}\bar{1}0\rangle$ split interstitial, the N-N dumbbell locates in the glide space and exactly arrows along the $\langle 2\bar{1}\bar{1}0\rangle$ direction with the bond length of 1.40 Å. It should be pointed out that Gao *et al.*[26] have improperly denoted N^+-N$\langle 01\bar{1}0\rangle$-g as N^+-N$\langle 2\bar{1}\bar{1}0\rangle$ split interstitial, since the description of this split interstitial in their literature[26], that each N atom of N-N dumbbell forms two bonds with the surrounding Ga atoms, is consistent with N^+-N$\langle 01\bar{1}0\rangle$-g rather than N^+-N$\langle 2\bar{1}\bar{1}0\rangle$ split interstitial. In N^+-Ga$\langle 01\bar{1}0\rangle$ split interstitial, the N-Ga dumbbell tilts by about 20° from the $\{0001\}$ towards the $\{03\bar{3}4\}$ plane as shown in Fig. 8 (h). The N-Ga dumbbell is in compressive state with the bond length of 1.80 Å shorter than the ideal N-Ga bonds in the perfect structure (1.96 Å along the c axis and 1.95 Å for the other three bonds in the c plane). Therefore, the structural description of N-N bonds in N split interstitials by the SW potential is more consistent with DFT calculations than the MEAM counterpart, which is similar to the investigation of IDB^H structure in Sec. III D.

In the exploration of Ga interstitials, Ga_{Oct}, Ga_{Tet} interstitials and Ga^+-Ga$\langle 01\bar{1}0\rangle$-e, Ga^+-Ga$\langle 2\bar{1}\bar{1}0\rangle$ split interstitials are produced by the SW potential as shown in Figs. 6 (i)-(l). Ga^+-Ga$\langle 01\bar{1}0\rangle$-e split interstitial is relaxed from the initial configurations of Ga^+-N$\langle 01\bar{1}0\rangle$ and Ga^+-Ga$\langle 01\bar{1}0\rangle$. Since the Ga-Ga dumbbell is nearly perpendicular to the $\{03\bar{3}4\}$ plane and binds with two neighboring N atoms to form a small tetrahedron analogous to the structure of N^+-N$\langle 01\bar{1}0\rangle$-e split interstitial, the index '-e' is added in the denotation of Ga^+-Ga$\langle 01\bar{1}0\rangle$-e split interstitial. The bond length of Ga-Ga dumbbell is 2.26 Å. The Ga^+-N$\langle 01\bar{1}0\rangle$-o and Ga^+-N$\langle 2\bar{1}\bar{1}0\rangle$ initial configurations are unstable and convert into Ga_{Oct} after the structural relaxation. Different from the case of N_{Tet}, the configuration of Ga_{Tet} is stable, where the Ga interstitial atom pushes the underlying host Ga-N pair downwards to bind with the below Ga atom, then a straight N-Ga-Ga-N-Ga atomic chain is formed along the c axis, which has been denoted as the bridge-bond geometry in the literature[74]. The interatomic distance of the N-Ga-Ga-N-Ga atomic chain is of 2.11 Å for the Ga-Ga pair and 1.80 Å for the host N-Ga pair. In Ga^+-Ga$\langle 2\bar{1}\bar{1}0\rangle$ split interstitial, the Ga-Ga dumbbell binds with two neighboring host Ga atoms in the same glide plane to form a curved Ga-Ga-

Ga-Ga atomic chain[26], and the mirror symmetry is preserved about the $\{2\overline{1}\overline{1}0\}$ plane same as N^+-N$\langle 2\overline{1}\overline{1}0\rangle$ split interstitial. The interatomic distance of the metal chain is of 2.40 Å, 2.31 Å and 2.40 Å, respectively.

Similar to the case of N interstitials, the MEAM potential predicts more configurations of Ga interstitials than the SW counterpart, which include Ga_{Oct} interstitial, Ga^+-Ga$\langle 01\overline{1}0\rangle$-e, Ga^+-N$\langle 01\overline{1}0\rangle$ Ga^+-N$\langle 01\overline{1}0\rangle$-o, Ga^+-Ga$\langle 01\overline{1}0\rangle$-g and Ga^+-Ga$\langle 2\overline{1}\overline{1}0\rangle$ split interstitials as shown in Figs. 7 (k)-(p). The initial configurations of Ga_{Oct} interstitial, Ga^+-N$\langle 01\overline{1}0\rangle$, Ga^+-N$\langle 01\overline{1}0\rangle$-o and Ga^+-Ga$\langle 2\overline{1}\overline{1}0\rangle$ split interstitials are preserved, while Ga_{Tet} interstitial is unstable and convert into Ga^+-Ga$\langle 01\overline{1}0\rangle$-e split interstitial (Fig. 7 (l)). The Ga^+-Ga$\langle 01\overline{1}0\rangle$ initial configuration is relaxed into Ga^+-Ga$\langle 01\overline{1}0\rangle$-g split interstitial as shown in Fig. 7 (o), where the Ga-Ga dumbbell tilts to be nearly parallel to the $\{03\overline{3}4\}$ plane analogous to the structure of N^+-N$\langle 01\overline{1}0\rangle$-g split interstitial, so that the index '-g' is added in this denotation. It should be noticed that one Ga atom of this Ga-Ga dumbbell binds with three but the other Ga atom binds with two neighboring N atoms. The bond length of Ga-Ga dumbbell is of 2.06 Å in Ga^+-Ga$\langle 01\overline{1}0\rangle$-e and 1.99 Å in Ga^+-Ga$\langle 01\overline{1}0\rangle$-g split interstitials, respectively. Besides the preserved candidate, the Ga^+-N$\langle 2\overline{1}\overline{1}0\rangle$ initial configuration converts into Ga^+-N$\langle 01\overline{1}0\rangle$ split interstitial as well after the structural relaxation. In the paired configurations of Ga^+-N$\langle 01\overline{1}0\rangle$ and Ga^+-N$\langle 01\overline{1}0\rangle$-o split interstitials, the N-Ga dipole points to the $\langle 01\overline{1}0\rangle$ and its reverse directions, respectively. In Ga^+-N$\langle 01\overline{1}0\rangle$ split interstitial, the interstitial Ga atom binds with the frontal host Ga atom and pushes it forwards to form a N-Ga-Ga crowdion in the $\{2\overline{1}\overline{1}0\}$ plane, where the Ga-Ga pair is roughly parallel to the $\{0\overline{3}38\}$ plane. In the N-Ga-Ga crowdion, the interatomic distance is of 2.12 Å for the Ga-Ga pair and 1.91 Å for the N-Ga dipole in compression, whereas the N-Ga dumbbell in Ga^+-N$\langle 01\overline{1}0\rangle$-o split interstitial has a bond length of 1.95 Å. In line with the result of SW potential, the MEAM potential produces a curved Ga-Ga-Ga-Ga atomic chain in Ga^+-Ga$\langle 2\overline{1}\overline{1}0\rangle$ split interstitial, where the interatomic distance between Ga atoms is of 2.43 Å, 2.08 Å and 2.43 Å, respectively.

The further structural relaxation of DFT calculations confirms five stable configurations of Ga interstitials, that are Ga_{Oct}, Ga_{Tet} interstitials, and Ga^+-Ga$\langle 01\overline{1}0\rangle$-g, Ga^+-N$\langle 01\overline{1}0\rangle$, Ga^+-Ga$\langle 2\overline{1}\overline{1}0\rangle$ split interstitials as shown in Figs. 8 (i)-(m). In Ga_{Oct} and Ga_{Tet} interstitials, C_{3v} symmetry is exactly preserved as discussed by Chow *et al.*[27]. Along the straight N-Ga-Ga-N-Ga atomic chain in Ga_{Tet} interstitial, the Ga-Ga bond length is 2.21 Å and

the host Ga-N pair is compressed to 1.78 Å. In Ga^{+}-Ga$\langle 01\overline{1}0\rangle$-g split interstitial (Fig. 8 (k)), the Ga-Ga dumbbell keeps nearly parallel to the $\{03\overline{3}4\}$ plane as well with the bond length of 2.16 Å. In Ga^{+}-N$\langle 01\overline{1}0\rangle$ split interstitial (Fig. 8 (l)), the N-Ga-Ga crowdion is preserved with the interatomic distance of 2.17 Å for the Ga-Ga pair and 1.77 Å for the N-Ga dipole in comparison. Same to the results of SW and MEAM potentials, the DFT-relaxed Ga^{+}-Ga$\langle 2\overline{1}\overline{1}0\rangle$ split interstitial is characterized by the Ga-Ga-Ga-Ga atomic chain as shown in Fig. 8 (m). The interatomic distance is of 2.38 Å, 2.33 Å and 2.38 Å along this metal chain, respectively.

Therefore, the atomic structures of native point defects in wurtzite GaN have been explored as completely as possible using the SW and MEAM potentials with the benchmark of DFT calculations. In viewpoint of the potential energy landscape, the MEAM potential predicts more local minima than either the SW counterpart or DFT calculations even though the three methods produce a intersection set of local minima for the same atomic configurations of native point defects. For the commonly predicted point defects, the structural features, typically the bond length of N-N and Ga-Ga dumbbells relaxed by the SW potential are more consistent with the results of DFT calculations than by the MEAM potential. The distinct mappings of the energy landscapes predicted by the two potentials could be understood intuitively based on their models of interatomic interaction as follows. In regard to covalent systems, the bonding configuration and the saturation of bonding number are explicitly determined by the three-body term in the SW potential (Eq. 2), while the directional characteristics of covalent bonds and the influence of atomic environments are implicitly described through the screening factor S_{ij} (Eq. 14 in Reference[40]) in the MEAM potential. The change of atomic structures is local in point defects. The SW potential could sensitively count this local change once the neighboring atoms are displaced, whereas in the calculation of MEAM potential, taking Ga^{+}-Ga$\langle 01\overline{1}0\rangle$ split interstitial as example, the contribution of screening factor S_{ij} would vary little when the Ga-Ga dumbbell rotates since the atomic environment around it is almost preserved, so that multiple stable configurations may exist with respect to the different orientations of Ga-Ga dumbbell, and thus the extra local minima appear in the energy landscape of MEAM potential.

The thermodynamical stability of neutral point defects are measured by the formation energy Ω defined as[26]

$$\Omega = E_{\mathrm{D}} - n_{\mathrm{N}}\mu_{\mathrm{N}} - n_{\mathrm{Ga}}\mu_{\mathrm{Ga}}, \tag{3}$$

where E_{D} is the total energy of defective structure containing n_{N} N atoms and n_{Ga} Ga atoms. μ_{N} and μ_{Ga} are the chemical potentials of Ga and N atoms, respectively. In the thermodynamic equilibrium, μ_{N} and μ_{Ga} are subject to the constraint condition of $\mu_{GaN} = \mu_N + \mu_{Ga}$ where μ_{GaN} is the chemical potential of GaN. Since the chemical potentials of elemental Ga bulk and N_2 molecule are not defined in the SW potential, the relative formation energy $\Delta\Omega$ is introduced instead as $\Delta\Omega = E_{\mathrm{D}} - E_{\mathrm{D},0}$ where $E_{\mathrm{D},0}$ is the total energy of reference structure. In this work, N^+-N$\langle 01\bar{1}0\rangle$-g and $\mathrm{Ga_{Oct}}$ configurations are taken as the reference structures for N and Ga interstitials, respectively.

The relative formation energies $\Delta\Omega$ calculated by the SW and MEAM potentials along with the DFT results are presented in Table V for the N and Ga interstitials shown in Figs. 6, 7 and 8. In the results of DFT calculations, N^+-N$\langle 01\bar{1}0\rangle$-g split interstitial is the most stable configuration thus to be taken as the ground state among N interstitials in line with the study of Bardeleben *et al*[19]. The new N^+-N$\langle 2\bar{1}\bar{1}0\rangle$ split interstitial is the second most stable configuration with 0.407 eV higher in energy, while the formation energy of N^+-N$\langle 01\bar{1}0\rangle$-e split interstitial is higher by 0.447 eV than its ground state N^+-N$\langle 01\bar{1}0\rangle$-g in agreement with the reported value of 0.35 eV[19]. The extra metastable configurations would imply new diffusion pathways for N interstitials in the process of migration and rearrangement. Different from DFT calculations, the SW potential predicts $\mathrm{N_{Oct}}$ interstitial to be the most stable configuration. Among the other three split interstitials, N^+-N$\langle 01\bar{1}0\rangle$-g has the lower formation energy than either N^+-N$\langle 2\bar{1}\bar{1}0\rangle$ or N^+-N$\langle 01\bar{1}0\rangle$-e configuration, which is consistent with the results of DFT calculations. Superior to the SW counterpart, the MEAM potential predicts N^+-N$\langle 01\bar{1}0\rangle$-g split interstitial as the most stable configuration in line with the DFT calculations. But the relative formation energies of other N interstitials, specially N^+-N$\langle 2\bar{1}\bar{1}0\rangle$ and N^+-N$\langle 01\bar{1}0\rangle$-e configurations are rather high in comparison with the results of DFT calculations, so that they will be hardly visited during the dynamic simulation of N interstitials. Regarding Ga interstitials, the DFT calculations indicate that $\mathrm{Ga_{Oct}}$ interstitial is the most stable configuration. And except Ga^+-Ga$\langle 2\bar{1}\bar{1}0\rangle$ split interstitial, the other Ga interstitials $\mathrm{Ga_{Tet}}$, Ga^+-Ga$\langle 01\bar{1}0\rangle$-g and Ga^+-N$\langle 01\bar{1}0\rangle$ have the relative formation energies less than 0.4 eV in comparison with $\mathrm{Ga_{Oct}}$. The SW potential correctly predicts $\mathrm{Ga_{Oct}}$ to be the most stable Ga interstitial in agreement with the DFT calculations, so that this version of SW potential presented in Table I is superior to that one used in the previous work[26]. On the other hand, rather different from the SW potential and DFT calculations, the MEAM

potential predicts Ga^{+}-Ga$\langle 01\bar{1}0\rangle$-e split interstitial to be the most stable configuration. But the formation energies of other Ga interstitials such as Ga^{+}-Ga$\langle 01\bar{1}0\rangle$-g and Ga^{+}-N$\langle 01\bar{1}0\rangle$ and Ga^{+}-Ga$\langle 2\bar{1}\bar{1}0\rangle$ are reasonably consistent with the values of DFT calculations. To conclude, neither SW nor MEAM potentials could individually perform very well to describe the interstitial point defects in GaN. However, they are complementary with respect to the structural and thermodynamical properties of those point defects, and it is worthy to use two potentials as a cross reference for the dynamical simulations of defective GaN.

B. Point defect complexes

In addition to the native point defects, their point defect complexes are further explored with respect to the interaction between two native point defects. Four point defect complexes are selected as follows. (1) Schottky, which is created by removing one N-Ga pair from GaN bulk. (2) Paired antisite $N_{Ga}Ga_N$, where the N and Ga atoms in one N-Ga pair occupy the opposite sites of each other. (3) Anion (Cation) octahedral Frenkel defect $Frenkel_{Oct}(N)$ ($Frenkel_{Oct}(Ga)$), where one N (Ga) atom is moved from its equilibrium site to the nearest octahedral space to form a N (Ga) vacancy plus a N (Ga) octahedral interstitial. Similarly, (4) N (Ga) tetrahedral Frenkel defect $Frenkel_{Tet}(N)$ ($Frenkel_{Tet}(Ga)$), which could be initially constructed by moving one host N (Ga) atom to the nearest tetrahedral site. But the configurations are unstable and recover back to the perfect structure after the structural relaxation using either the SW potential or DFT calculation, so that they are not considered further here.

The relaxed atomic structures of point defect complexes are shown in Fig. 9 with respect to three methods. In details, Figs. 9 (a1)-(a3) manifest no structural collapse in the Schottky defect. There is just a slight expansion around Ga vacancy and a little shrinkage around N vacancy in the atomic structures relaxed by the DFT calculation and MEAM potential, and hardly any deformation in the calculation of SW potential. However, the DFT calculations reveal that both of the initial configurations of $N_{Ga}Ga_N$ and $Frenkel_{Oct}(N)$ defects are unstable, and they similarly convert into the point defect complexes made up of N vacancy and N^{+}-N$\langle 01\bar{1}0\rangle$-g split interstitial, where the distance between the two native point defects is approximately of $1.4a$ (Fig. 9 (b1)) and $2.4a$ (Fig. 9 (c1)) (a: lattice constant), respectively. The symbol of '$\oplus$' is adopted as the linkage in point defect complexes. Thus the relaxed

structures of $N_{Ga}Ga_N$ and $Frenkel_{Oct}(N)$ defects are denoted as $(V_N \oplus N^+\text{-}N\langle 01\bar{1}0\rangle\text{-g})_{1.4a}$ and $(V_N \oplus N^+\text{-}N\langle 01\bar{1}0\rangle\text{-g})_{2.4a}$, respectively. In contrast, the initial configuration of $N_{Ga}Ga_N$ is preserved in the structural relaxation of SW and MEAM potentials as shown in Figs. 9 (b2) and (b3), respectively. Furthermore, the DFT-relaxed structure (Fig. 9 (b1)) is taken as the initial configuration to be relaxed by the SW and MEAM potentials for $N_{Ga}Ga_N$ defect. In the calculation of SW potential, the interstitial configuration of N-N dumbbell in $(V_N \oplus N^+\text{-}N\langle 01\bar{1}0\rangle\text{-g})_{1.4a}$ is replaced by a nearly horizontal N-Ga dumbbell as shown in Fig. 9 (b2'), which could be equivalently formed by rotating a vertical N-Ga pair by about 90° in the perfect structure similar to the formation of Stones-Wales defect in graphite[75]. Meanwhile, the initial configuration of $(V_N \oplus N^+\text{-}N\langle 01\bar{1}0\rangle\text{-g})_{1.4a}$ is preserved for the MEAM potential as shown in Fig. 9 (b3'). The interatomic distance of N-N pair is of 1.42 Å, 1.58 Å and 1.12 Å in the atomic structures relaxed by the DFT calculation, SW and MEAM potentials, respectively. The initial configuration of $Frenkel_{Oct}(N)$ is preserved in the structural relaxation of SW and MEAM potentials as well, but just only the interstitial N atom stays at an off-center site in the octahedral space restricted by six neighboring Ga atoms as shown in Figs. 9 (c2) and (c3), respectively. Similar to the case of $N_{Ga}Ga_N$, taking the DFT-relaxed structure (Fig. 9 (c1)) as the initial configuration, $(V_N \oplus N^+\text{-}N\langle 01\bar{1}0\rangle\text{-g})_{2.4a}$ point defect complexes are preserved in the structural relaxation of SW and MEAM potentials as shown in Figs. 9 (c2') and (c3'), respectively. The geometric features of N-N dumbbells are restored as those in the isolated $N^+\text{-}N\langle 01\bar{1}0\rangle$-g split interstitials shown in Fig. 8 (e) for DFT calculation, in Fig. 6 (e) for SW and in Fig. 7 (e) for MEAM potentials, respectively. The bond length of N-N dumbbell is correspondingly of 1.44 Å, 1.35 Å and 1.11 Å in the relaxed structures of DFT calculation, SW and MEAM potentials. Different from $Frenkel_{Oct}(N)$, the initial configuration of $Frenkel_{Oct}(Ga)$ is preserved for three methods as shown in Figs. 9 (d1)-(d3). The interstitial Ga atom occupies the body center of octahedral space closely adjacent the Ga vacancy, and the distance between two point defects is approximately of $2\sqrt{3}/3a$ (a: lattice constant).

Since $n_N = n_{Ga}$ in the investigated point defect complexes, Eq. 3 could be simplified as

$$\Omega = E_D - E_0, \tag{4}$$

where E_0 is the total energy of perfect structure with the same atomic number to the defective system for each elemental species. The corresponding formation energies of the

point defect complexes shown in Fig. 9 are listed in Table VI, which are arranged according to the values of DFT calculations in ascending order. If only considering the $V_N \oplus N^+$-N$\langle 01\bar{1}0\rangle$-g configurations instead of either Frenkel$_{Oct}$(N) or $N_{Ga}Ga_N$, the three methods roughly agree for the tendency of thermodynamical stability of defective structures, that Schottky is the most stable point defect complex, followed by $(V_N \oplus N^+$-N$\langle 01\bar{1}0\rangle$-g$)_{2.4a}$ ($(V_N \oplus N^+$-N$\langle 01\bar{1}0\rangle$-g$)_{1.4a}$), and Frenkel$_{Oct}$(Ga) has the highest formation energy. Moreover, except $(V_N \oplus N^+$-N$\langle 01\bar{1}0\rangle$-g$)_{2.4a}$ the formation energies of those defects calculated by the SW potential are quantitatively more consistent with the DFT results than the MEAM counterpart.

On the other hand, the interaction between two native point defects in the point defect complex is further investigated by considering the system, where two native point defects locate with an infinite separation. And the corresponding formation energy could be simply calculated by summing those of two isolated point defects. In order to be compatible with the configurations of those point defect complexes discussed above, four paired point defects are modeled as follows $V_N + V_{Ga}$, $V_N + N^+$-N$\langle 01\bar{1}0\rangle$-g, $N_{Ga} + Ga_N$ and $V_{Ga} + Ga_{Oct}$, where the symbol of '+' is adopted in place of '$\oplus$' to signify the infinite separation between two point defects. Similar to the point defect complexes, the formation energies of them are calculated with Eq. 4 due to the equal atomic number of Ga and N species. The results are presented in Table VI for the three methods. The DFT calculations reveal that the formation energy reduces when the distance between two point defects decreases. For instance, the formation energy reduces by 3.544 eV in the formation of Schottky defect from $V_N + V_{Ga}$, and by 4.879 eV in the formation of Frenkel$_{Oct}$(Ga) from $V_{Ga} + Ga_{Oct}$. Beginning with the paired point defect of $V_N + N^+$-N$\langle 01\bar{1}0\rangle$-g (or $N_{Ga} + Ga_N$), the formation energy reduces by 0.716 eV (or 6.572 eV) when two isolated point defects move close to form $(V_N \oplus N^+$-N$\langle 01\bar{1}0\rangle$-g$)_{2.4a}$. Thus the point defect complexes, at least those listed in Table VI, are energetically feasible rather than dissociate into two isolated point defects. The energy tendency predicted by the DFT calculations is reasonably reproduced by the SW potential, that the formation energy reduces by 2.176 eV in the formation of Schottky from $V_N + V_{Ga}$, by 0.016 eV or 3.363 eV in the formation of $(V_N \oplus N^+$-N$\langle 01\bar{1}0\rangle$-g$)_{2.4a}$ from $V_N + N^+$-N$\langle 01\bar{1}0\rangle$-g or $N_{Ga} + Ga_N$, and by 0.025 eV in the formation of Frenkel$_{Oct}$(Ga) from $V_{Ga} + Ga_{Oct}$, respectively. But the MEAM potential wrongly predicts the dissociation of Schottky and $(V_N \oplus N^+$-N$\langle 01\bar{1}0\rangle$-g$)_{2.4a}$ ($(V_N \oplus N^+$-N$\langle 01\bar{1}0\rangle$-g$)_{1.4a}$) point defect complexes

to be exothermic by the energy reduction of 0.034 eV for the former and of 0.024 eV (0.072 eV) for the latter, respectively. Therefore, the point defect complexes including Schottky, $(V_N \oplus N^+\text{-}N\langle 01\bar{1}0\rangle\text{-g})_{2.4a}$ ($(V_N \oplus N^+\text{-}N\langle 01\bar{1}0\rangle\text{-g})_{1.4a}$) and $\text{Frenkel}_{\text{Oct}}(\text{Ga})$ are thermodynamically stable rather than dissociating into two isolated point defects as predicted by the DFT calculations and SW potential with respect to the interaction between them.

V. SUMMARY

In summary, the Stillinger-Weber potential is modified for GaN with the explicit consideration of N-Ga-N (N-N-Ga) and Ga-Ga-N (Ga-N-Ga) triplets besides the regular N-Ga-Ga (Ga-N-N), N-N-N and Ga-Ga-Ga terms. The fundamental properties of wurtzite GaN including the lattice parameters, elastic constants and lattice dynamics are reproduced by the SW and MEAM potentials. Due to the lack of long-range (e.g. electrostatic) interaction, the LO-TO splitting in the phonon dispersion could be hardly described by both potentials. The investigation of inversion domain boundaries indicates that the SW potential is reliable to describe the defective structures involving N-N and Ga-Ga bonds, while the MEAM potential is more transferable than the SW counterpart in the structural transformation, such as the wurtzite-rocksalt phase transition where the atomic environments change apparently. The combination of SW and MEAM potentials with DFT calculation is efficient in the structural search of native point defects in GaN. Two N and two Ga split interstitials are first obtained in this work that are $N^+\text{-}N\langle 2\bar{1}\bar{1}0\rangle$, $N^+\text{-}Ga\langle 01\bar{1}0\rangle$ and $Ga^+\text{-}Ga\langle 01\bar{1}0\rangle$-g, $Ga^+\text{-}N\langle 01\bar{1}0\rangle$ configurations after the refinement of DFT calculations from the candidates relaxed by the SW and MEAM potentials, beside reproducing those already reported N (Ga) vacancies and antisites, $N^+\text{-}N\langle 01\bar{1}0\rangle$-g and $N^+\text{-}N\langle 01\bar{1}0\rangle$-e N split interstitials, as well as Ga_{Oct}, Ga_{Tet} and $Ga^+\text{-}Ga\langle 2\bar{1}\bar{1}0\rangle$ configurations of Ga interstitials. However, neither of SW and MEAM potentials produces simultaneously the most stable N and Ga interstitials. The present SW potential correctly predicts the octahedral occupation Ga_{Oct} as the most stable configuration of Ga interstitial superior to the previous version[26,38], while the MEAM potential exactly produces $N^+\text{-}N\langle 01\bar{1}0\rangle$-g to be the most stable N split interstitial. On a whole, the SW potential establishes less local minima than the MEAM counterpart in the potential energy landscape with respect to the configurations of interstitials, whereas the structural features of point defects concerning N-N or Ga-Ga bonds relaxed by the

SW potential are more consistent with the results of DFT calculations than those by the MEAM potential. In regard to the point defect complexes, the Schottky and $\text{Frenkel}_{\text{Oct}}(\text{Ga})$ configurations are preserved, but $\text{Frenkel}_{\text{Oct}}(\text{N})$ and $\text{N}_{\text{Ga}}\text{Ga}_{\text{N}}$ are unstable and convert into $(\text{V}_{\text{N}} \oplus \text{N}^{+}\text{-N}\langle 01\bar{1}0\rangle\text{-g})_{2.4a}$ and $(\text{V}_{\text{N}} \oplus \text{N}^{+}\text{-N}\langle 01\bar{1}0\rangle\text{-g})_{1.4a}$ point defect complexes in the DFT calculations, respectively. In general, three methods consistently demonstrate that Schottky is the most stable followed by $\text{V}_{\text{N}} \oplus \text{N}^{+}\text{-N}\langle 01\bar{1}0\rangle\text{-g}$ (either $(\text{V}_{\text{N}} \oplus \text{N}^{+}\text{-N}\langle 01\bar{1}0\rangle\text{-g})_{2.4a}$ or $(\text{V}_{\text{N}} \oplus \text{N}^{+}\text{-N}\langle 01\bar{1}0\rangle\text{-g})_{1.4a}$) in the studied point defect complexes, and $\text{Frenkel}_{\text{Oct}}(\text{Ga})$ has the highest formation energy. Furthermore, the formation energies calculated by DFT and SW potential indicate that all of the point defect complexes are energetically favorable rather than dissociating into two isolated point defects. But the MEAM potential wrongly predicts that the dissociation of Schottky and $\text{V}_{\text{N}} \oplus \text{N}^{+}\text{-N}\langle 01\bar{1}0\rangle\text{-g}$ point defect complexes is exothermic. This work suggests that the present version of SW potential is applicable to simulate the dynamical properties of defective GaN on a large scale with a caution special to N interstitials. The mutual complementation with the MEAM potential would be a practical way for getting more accurate results. Finally, the newly explored N and Ga split interstitials could be useful in the study of diffusion pathways of point defects in GaN as possible intermediate states, and the identification of point defects in Al(In)N alloys.

ACKNOWLEDGMENTS

The author (Huaping LEI) acknowledges the supports of the China Scholarship Council [Grant No. 201904910166]. This project has received the funding from the European Union's Horizon 2020 research and innovation programme under the Marie Skłodowska-Curie grant agreement No. 101034329 and the financial support from the WINNINGNormandy programme of the Normandy Region [Contract No. 013C256P]. All authors also acknowledge the support of Région Normandie Project "RIN 2018 PLACENANO" [Convention No. 18E01651]. All of calculations were implemented in CRIANN (Centre Régional Informatique et d'Applications Numériques de Normandie) under the projects No. 2016009 and 2021006.

REFERENCES

[1]I. Akasaki and H. Amano, Japanese Journal of Applied Physics **45**, 9001 (2006).

[2]A. Ionascut-Nedelcescu, C. Carlone, A. Houdayer, H. J. von Bardeleben, J. L. Cantin, and S. Raymond, IEEE Transactions on Nuclear Science **49**, 2733 (2002).

[3]P. Ruterana, M. Albrecht, and J. Neugebauer, eds., Nitride semiconductors: Handbook on materials and devices (John Wiley & Sons, Ltd, 2003) Chap. 11-13, pp. 529–660.

[4]S. Nakamura, Journal of Vacuum Science & Technology A **13**, 705 (1995).

[5]S. Nakamura, M. Senoh, S.-I. Nagahama, N. Iwasa, T. Yamada, T. Matsushita, H. Kiyoku, and Y. Sugimoto, Japanese Journal of Applied Physics **35**, L74 (1996).

[6]S. Nakamura, Semiconductor Science and Technology **14**, R27 (1999).

[7]M. Meneghini, A. Tajalli, P. Moens, A. Banerjee, E. Zanoni, and G. Meneghesso, Materials Science in Semiconductor Processing **78**, 118 (2018).

[8]B. Setera and A. Christou, Microelectronics Reliability **124**, 114336 (2021).

[9]J. P. Hirth and J. Lothe, Theory of dislocations (Wiley-Interscince Publication, New York, 1992) Chap. 14, pp. 487–530, 2nd ed.

[10]J. K. Sheu and G. C. Chi, Journal of Physics: Condensed Matter **14**, R657 (2002).

[11]S. J. Pearton, R. Deist, F. Ren, L. Liu, A. Y. Polyakov, and J. Kim, Journal of Vacuum Science & Technology A **31**, 050801 (2013).

[12]S. J. Pearton, Y.-S. Hwang, and F. Ren, JOM **67**, 1601 (2015).

[13]K. Kanegae, H. Fujikura, Y. Otoki, T. Konno, T. Yoshida, M. Horita, T. Kimoto, and J. Suda, Applied Physics Letters **115**, 012103 (2019).

[14]M. A. Reshchikov and H. Morkoç, Journal of Applied Physics **97**, 061301 (2005).

[15]J. Neugebauer and C. G. Van de Walle, Physical Review B **50**, 8067 (1994).

[16]A. Y. Polyakov, S. J. Pearton, P. Frenzer, F. Ren, L. Liu, and J. Kim, Journal of Materials Chemistry C **1**, 877 (2013).

[17]R. Wang, X. Tong, J. Xu, C. Dong, Z. Cheng, L. Zhang, S. Zhang, P. Zheng, F.-X. Chen, Y. Zhang, and W. Tan, Physical Review Applied **14**, 024039 (2020).

[18]R. Wang, J. Xu, S. Zhang, Y. Zhang, P. Zheng, Z. Cheng, L. Zhang, F.-X. Chen, X. Tong, Y. Zhang, and W. Tan, Journal of Materials Chemistry C **9**, 3177 (2021).

[19]H. J. von Bardeleben, J. L. Cantin, U. Gerstmann, A. Scholle, S. Greulich-Weber, E. Rauls, M. Landmann, W. G. Schmidt, A. Gentils, J. Botsoa, and M. F. Barthe, Physical Review Letters **109**, 206402 (2012).

[20]H. J. von Bardeleben, J. L. Cantin, H. Vrielinck, F. Callens, L. Binet, E. Rauls, and U. Gerstmann, Physical Review B **90**, 085203 (2014).

[21]J. L. Lyons and C. G. Van de Walle, npj Computational Materials **3**, 12 (2017).

[22]Y. Gao, D. Sun, X. Jiang, and J. Zhao, Journal of Applied Physics **125**, 215705 (2019).

[23]Z. Xie, Y. Sui, J. Buckeridge, C. R. A. Catlow, T. W. Keal, P. Sherwood, A. Walsh, M. R. Farrow, D. O. Scanlon, S. M. Woodley, and A. A. Sokol, Journal of Physics D: Applied Physics **52**, 335104 (2019).

[24]J. L. Lyons, D. Wickramaratne, and C. G. Van de Walle, Journal of Applied Physics **129**, 111101 (2021).

[25]H. He, W. Liu, P. Zhang, W. Liao, D. Tong, L. Yang, C. He, H. Zang, and H. Zong, Materials **13**, 3627 (2020).

[26]F. Gao, E. J. Bylaska, and W. J. Weber, Physical Review B **70**, 245208 (2004).

[27]K. H. Chow, G. D. Watkins, A. Usui, and M. Mizuta, Physical Review Letters **85**, 2761 (2000).

[28]I. C. Diallo and D. O. Demchenko, Physical Review Applied **6**, 064002 (2016).

[29]S. Hautakangas, J. Oila, M. Alatalo, K. Saarinen, L. Liszkay, D. Seghier, and H. P. Gislason, Physical Review Letters **90**, 137402 (2003).

[30]S. Limpijumnong and C. G. Van de Walle, Physical Review B **69**, 035207 (2004).

[31]A. Kyrtsos, M. Matsubara, and E. Bellotti, Physical Review B **93**, 245201 (2016).

[32]K. Saarinen, T. Suski, I. Grzegory, and D. C. Look, Physical Review B **64**, 233201 (2001).

[33]H. Lei, J. Chen, and P. Ruterana, Applied Physics Letters **96**, 161901 (2010).

[34]H. Lei, J. Chen, and P. Ruterana, Journal of Applied Physics **108**, 103503 (2010).

[35]M. K. Horton, S. Rhode, S.-L. Sahonta, M. J. Kappers, S. J. Haigh, T. J. Pennycook, C. J. Humphreys, R. O. Dusane, and M. A. Moram, Nano Letters **15**, 923 (2015).

[36]F. C.-P. Massabuau, S. L. Rhode, M. K. Horton, T. J. O'Hanlon, A. Kovacs, M. S. Zielinski, M. J. Kappers, R. E. Dunin-Borkowski, C. J. Humphreys, and R. A. Oliver, Nano Letters **17**, 4846 (2017).

[37]N. Aïchoune, V. Potin, P. Ruterana, A. Hairie, G. Nouet, and E. Paumier, Computational Materials Science **17**, 380 (2000).

[38]A. Béré and A. Serra, Physical Review B **65**, 205323 (2002).

[39]X. W. Zhou, R. E. Jones, and K. Chu, Journal of Applied Physics **122**, 235703 (2017).

[40]E. C. Do, Y.-H. Shin, and B.-J. Lee, Journal of Physics: Condensed Matter **21**, 325801 (2009).

[41]J. Nord, K. Albe, P. Erhart, and K. Nordlund, Journal of Physics: Condensed Matter **15**, 5649 (2003).

[42]J. Chen, P. Ruterana, and G. Nouet, Materials Science and Engineering: B **82**, 117 (2001).

[43]I. Belabbas, A. Béré, J. Chen, S. Petit, M. A. Belkhir, P. Ruterana, and G. Nouet, Physical Review B **75**, 115201 (2007).

[44]J. Kioseoglou, G. P. Dimitrakopulos, P. Komninou, and T. Karakostas, Physical Review B **70**, 035309 (2004).

[45]J. Chen, P. Ruterana, and G. Nouet, Physical Review B **67**, 205210 (2003).

[46]A. Béré and A. Serra, Physical Review B **68**, 033305 (2003).

[47]F. H. Stillinger and T. A. Weber, Physical Review B **31**, 5262 (1985).

[48]A directed grid search algorithm is used, where the guessed value and the variation range for each parameter are set initially, then the parameter is changed step by step as far as the calculated properties approach the selected references, otherwise the next parameter is set to be optimized similarly. This process is repeated until no better results are obtained.

[49]D. B. Holt, Journal of Physics and Chemistry of Solids **30**, 1297 (1969).

[50]J. E. Northrup, J. Neugebauer, and L. T. Romano, Physical Review Letters **77**, 103 (1996).

[51]A. Zoroddu, F. Bernardini, P. Ruggerone, and V. Fiorentini, Physical Review B **64**, 045208 (2001).

[52]J. E. Huheey, E. A. Keiter, and R. L. Keiter, *Inorganic Chemistry: Principles of Structure and Reactivity*, 4th ed. (Harper Collins College Publishers, New York, 1997).

[53]C. Kittel, *Introduction to Solid State Physics*, 8th ed. (John Wiley & Sons Inc., Hoboken, New Jersey, 2005).

[54]`https://lammps.sandia.gov`.

[55]G. Kresse and J. Furthmüller, Physical Review B **54**, 11169 (1996).

[56]P. E. Blöchl, Physical Review B **50**, 17953 (1994).

[57]J. P. Perdew, K. Burke, and M. Enzerhof, Physical Review Letters **77**, 3865 (1996).

[58]M. Leszczynski, H. Teisseyre, T. Suski, I. Grzegory, M. Bockowski, J. Jun, S. Porowski, K. Pakula, J. M. Baranowski, C. T. Foxon, and T. S. Cheng, Applied Physics Letters **69**, 73 (1996).

[59]K. Adachi, H. Ogi, A. Nagakubo, N. Nakamura, M. Hirao, M. Imade, M. Yoshimura, and Y. Mori, Journal of Applied Physics **119**, 245111 (2016).

[60]B. Fultz, Progress in Materials Science **55**, 247 (2010).

[61]L. T. Kong, C. Denniston, and M. H. Müser, Computer Physics Communications **182**, 540 (2011).

[62]L. T. Kong, Computer Physics Communications **182**, 2201 (2011).

[63]C. Campañá and M. H. Müser, Physical Review B **74**, 075420 (2006).

[64]The other sizes have been tested as well, such as $5a \times 5a \times 3c$, $10a \times 10a \times 6c$, $15a \times 15a \times 9c$ and $12a \times 12a \times 12c$.

[65]T. Schneider and E. Stoll, Physical Review B **17**, 1302 (1978).

[66]T. Ruf, J. Serrano, M. Cardona, P. Pavone, M. Pabst, M. Krisch, M. D'Astuto, T. Suski, I. Grzegory, and M. Leszczynski, Physical Review Letters **86**, 906 (2001).

[67]V. Y. Davydov, Y. E. Kitaev, I. N. Goncharuk, A. N. Smirnov, J. Graul, O. Semchinova, D. Uffmann, M. B. Smirnov, A. P. Mirgorodsky, and R. A. Evarestov, Physical Review B **58**, 12899 (1998).

[68]K. Kim, W. R. L. Lambrecht, and B. Segall, Physical Review B **53**, 16310 (1996).

[69]L. T. Romano, J. E. Northrup, and M. A. O'Keefe, Applied Physics Letters **69**, 2394 (1996).

[70]V. Potin, G. Nouet, and P. Ruterana, Applied Physics Letters **74**, 947 (1999).

[71]The cohesive energy and the equilibrium distance are 2.90 eV and 3.00 Å for Ga-Ga bonds, respectively.

[72]M. Ueno, M. Yoshida, A. Onodera, O. Shimomura, and K. Takemura, Physical Review B **49**, 14 (1994).

[73]J. Cai and N. Chen, Physical Review B **75**, 134109 (2007).

[74]P. Bogusławski, E. L. Briggs, and J. Bernholc, Physical Review B **51**, 17255(R) (1995).

[75]A. J. Stone and D. J. Wales, Chemical Physics Letters **128**, 501 (1986).

[76]K. Momma and F. Izumi, Journal of Applied Crystallography **44**, 1272 (2011).

TABLE I. Parameters of Stillinger-Weber potential for GaN in the format of i-j-k triplet, where i is the central atom. The units of ϵ and σ are eV and Å, respectively. The parameters $\gamma = 1.2$, $p = 4$ and $q = 0$ are preserved for all triplets.

Parameters	ϵ	σ	a	λ	A	B
N-Ga-Ga, Ga-N-N	2.2645	1.704	1.8	33.0	7.41825	0.69375
N-N-N	1.7368	1.400	1.8	13.0	4.41825	0.39375
Ga-Ga-Ga	1.4050	2.060	1.6	10.0	8.41825	1.09375
N-Ga-N, N-N-Ga	1.9832	1.400	1.8	13.0	5.72501	0.52265
Ga-Ga-N, Ga-N-Ga	1.7837	2.060	1.6	10.0	7.90245	0.87108

TABLE II. Lattice parameters a (Å), c (Å) and internal structural parameter u, as well as elastic constants C_{ij} (GPa) and bulk modulus B (GPa) of wurtzite GaN calculated by the SW and MEAM potentials in comparison with the experimental data.

GaN	Expt.	SW	MEAM
Lattice parameters			
a	3.189[a]	3.190	3.168
c	5.186[a]	5.210	5.173
c/a	1.626[a]	1.633	1.633
u	0.377[a]	0.375	0.375
Elastic parameters			
C_{11}	359.7[b]	364.7	350.6
C_{33}	391.8[b]	380.6	397.3
C_{44}	99.6[b]	107.3	93.0
C_{12}	129.9[b]	129.8	148.1
C_{13}	104.6[b]	113.9	101.4
C_{66}	114.9[b]	117.4	101.3
B	198.8[b]	202.8	200.0

[a] High-resolution x-ray diffraction[58].

[b] ATAR experiment[59].

802 TABLE III. Phonon frequencies (0.1 K) at some high-symmetry k points of wurtzite GaN calculated
803 by the SW and MEAM potentials in comparison with IXS (300 K)[66] and Raman scattering (6K)
804 experiments[67] and DFPT calculations[66]. All frequencies are given in THz.

k points	Mode	IXS[66]	Raman[67]	DFPT[66]	SW	MEAM
Γ	E1(LO)		22.3	22.6	25.8	26.4
Γ	A1(LO)	21.9	22.1	22.5	25.7	26.2
Γ	B1	20.7		21.6	25.5	26.0
Γ	E2		17.1	17.4	24.9	25.9
Γ	E1(TO)		16.8	17.1	24.4	25.3
Γ	A1(TO)		16.0	16.3	23.6	24.8
Γ	B1(low)	9.9		10.2	10.5	10.3
Γ	E2(low)		4.3	4.3	5.4	4.8
A	LO	21.3		22.0	25.2	26.1
A	LA	6.9		7.2	7.1	7.1
M	A1(TO)	17.3		18.0	22.9	21.4
M	E2	7.1		7.2	8.7	7.5
M	E2(low)	5.8		6.0	7.5	6.7
M	TA_z	5.5		5.6	6.4	5.6
M	TA_x	4.1		4.2	5.5	4.8
K	TO	18.4		18.8	22.0	20.3
K	TA	6.4		6.5	7.6	6.6

805

TABLE IV. Physical properties of IDB structures calculated by the SW and MEAM potentials in comparison with DFT calculations[50]. (Note: values listed are the formation energy $E_{\rm form}$ (meV/Å), bond length (Å) of N-N ($R_{\rm NN}$) and Ga-Ga ($R_{\rm GaGa}$) bonds in IDB$^{\rm H}$, as well as the averaged bond length (Å) of N-Ga bonds ($R_{4-\rm fold}$) in 4-fold atomic rings of IDB*.)

Properties	DFT[50]	SW	MEAM
IDB$^{\rm H}$			
$E_{\rm form}$	167	164	161
$R_{\rm NN}$	1.51	1.57	1.19
$R_{\rm GaGa}$	2.28	2.33	2.05
IDB*			
$E_{\rm form}$	25	60	19
$R_{4-\rm fold}$	1.94	2.00	1.95

TABLE V. Relative formation energies $\Delta\Omega$ (eV) of N and Ga interstitials calculated by the SW and MEAM potentials along with the DFT results. N^+-N$\langle 01\bar{1}0\rangle$-g and Ga_{Oct} configurations are taken as the reference structures for N and Ga interstitials, respectively.

Configurations	SW	MEAM	DFT
N interstitials			
N^+-N$\langle 01\bar{1}0\rangle$-g	0	0	0
N^+-N$\langle 2\bar{1}\bar{1}0\rangle$	0.310	3.363	0.407
N^+-N$\langle 01\bar{1}0\rangle$-e	0.117	0.864	0.447
N^+-Ga$\langle 01\bar{1}0\rangle$		6.109	3.083
N_{Oct}	-0.913	4.091	
N_{Tet}		2.750	
Ga interstitials			
Ga_{Oct}	0	0	0
Ga_{Tet}	2.402		0.237
Ga^+-Ga$\langle 01\bar{1}0\rangle$-g		0.423	0.281
Ga^+-Ga$\langle 01\bar{1}0\rangle$-e	0.105	-0.513	
Ga^+-N$\langle 01\bar{1}0\rangle$		0.363	0.391
Ga^+-N$\langle 01\bar{1}0\rangle$-o		0.373	
Ga^+-Ga$\langle 2\bar{1}\bar{1}0\rangle$	0.484	0.899	1.407

TABLE VI. Formation energies Ω (eV) (Eq. 4) of point defect complexes and paired point defects calculated by DFT as well as the SW and MEAM potentials, respectively.

Configurations	DFT	SW	MEAM
Point defect complexes			
Schottky	6.669	6.530	4.148
$\text{Frenkel}_{\text{Oct}}(\text{N})$		8.680^a	9.443^a
$(\text{V}_\text{N} \oplus \text{N}^+\text{-N}\langle 01\bar{1}0\rangle\text{-g})_{2.4a}$	7.328	9.848^b	5.519^b
$\text{N}_\text{Ga}\text{Ga}_\text{N}$		8.605^a	13.076^a
$(\text{V}_\text{N} \oplus \text{N}^+\text{-N}\langle 01\bar{1}0\rangle\text{-g})_{1.4a}$	7.497	7.207^b	5.567^b
$\text{Frenkel}_{\text{Oct}}(\text{Ga})$	10.071	10.456	6.072
Paired point defects			
$\text{V}_\text{N} + \text{V}_\text{Ga}$	10.213	8.706	4.114
$\text{V}_\text{N} + \text{N}^+\text{-N}\langle 01\bar{1}0\rangle\text{-g}$	8.044	9.864	5.495
$\text{N}_\text{Ga} + \text{Ga}_\text{N}$	13.900	13.211	13.152
$\text{V}_\text{Ga} + \text{Ga}_\text{Oct}$	14.950	10.481	6.136

[a] Preserved atomic structures.

[b] DFT-relaxed structure as initial configuration.

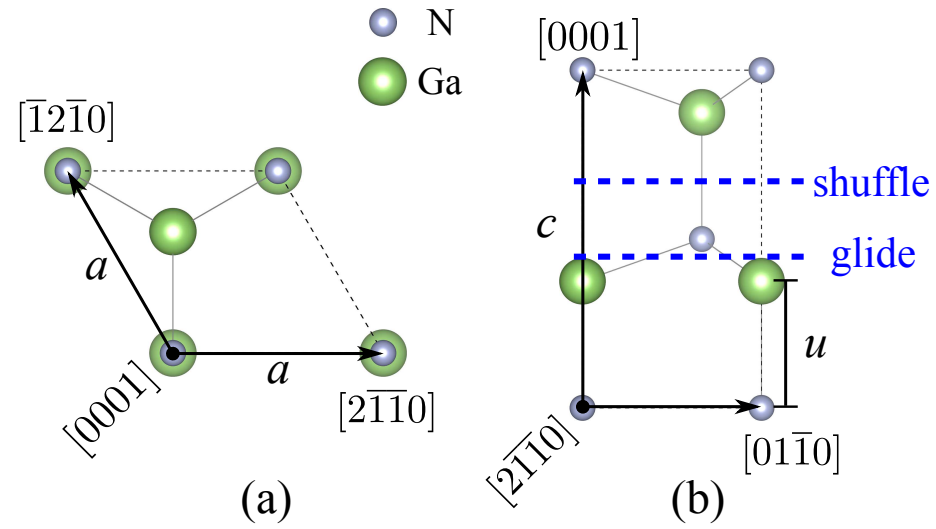

FIG. 1. (Color online) Sketch of the primitive cell of wurtzite GaN. (a) [0001] projection. (b) [$2\bar{1}\bar{1}0$] projection. Small gray and large green balls represent N and Ga atoms, respectively. a, c and u are the lattice constants and internal structural parameter, respectively. The glide and shuffle spaces along the [0001] plane are labeled out. VESTA[76] is used for visualization.

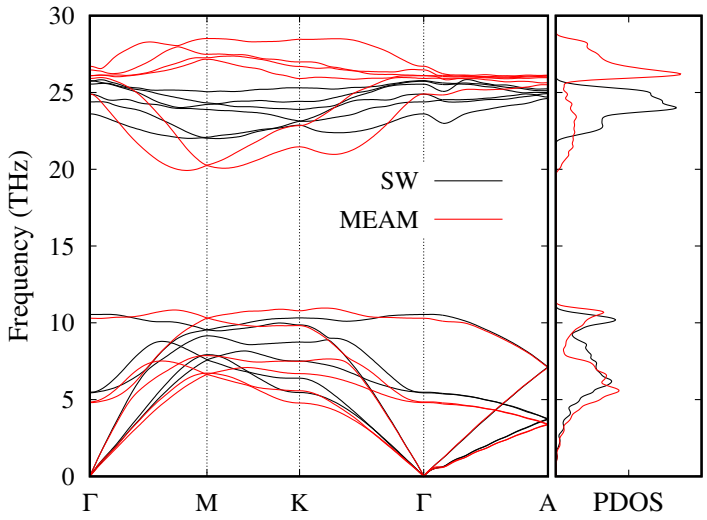

FIG. 2. (Color online) Phonon dispersion relationship of wurtzite GaN along the high symmetry lines of Brillouin zone at 0.1 K calculated by the SW and MEAM potentials, respectively.

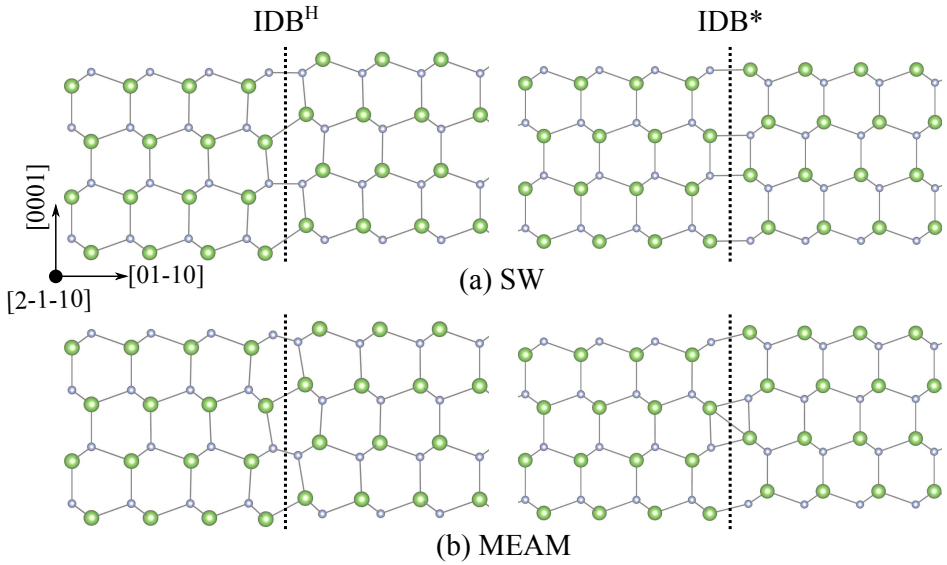

826

827 FIG. 3. (Color online) Atomic structures of IDB^H (Left) and IDB^* (Right) in wurtzite GaN
828 calculated by (a) SW and (b) MEAM potentials, respectively. The boundaries are indicated by
829 the dashed lines. The atomic representations are the same as in Fig. 1.

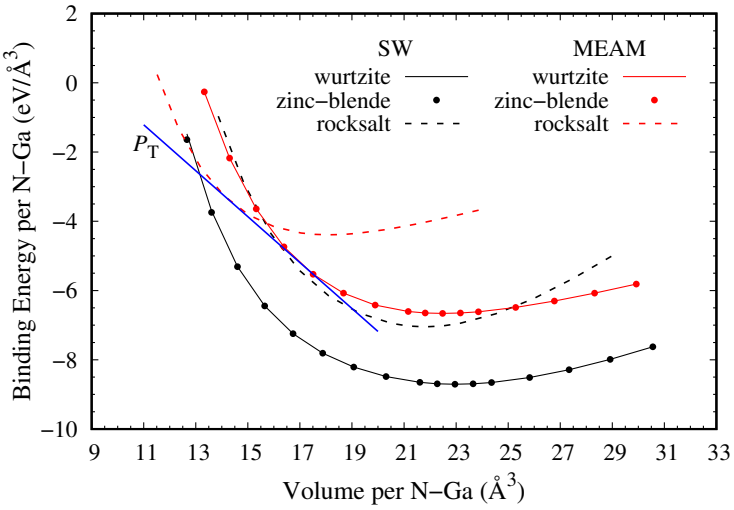

830

831 FIG. 4. (Color online) Volume dependence of binding energy in wurtzite, zinc-blende and rock-
832 salt lattices per formula unit (Ga-N) calculated by the SW (block) and MEAM (red) potentials,
833 respectively. P_T is the equilibrium transition pressure of wurtzite-rocksalt phase transition, which
834 is estimated to be 106 GPa by the MEAM potential.

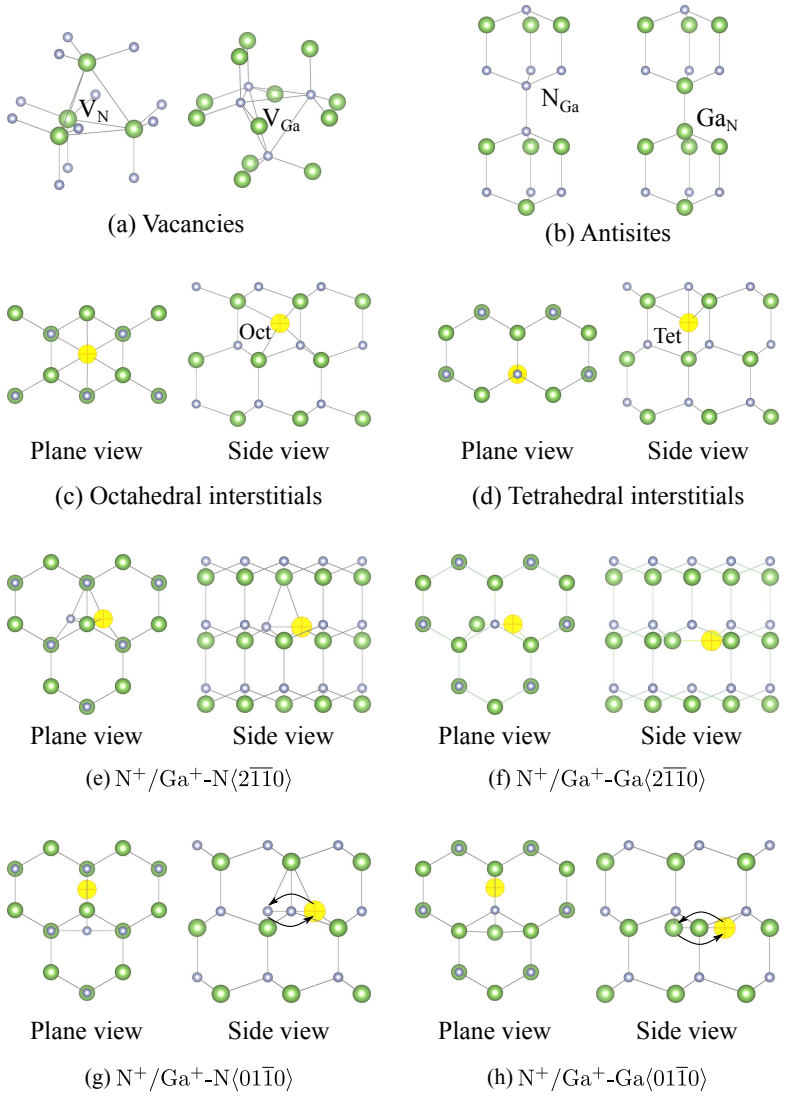

FIG. 5. (Color online) Illustrations of initial atomic configurations of native point defects in wurtzite GaN. (a) Vacancies, V_N and V_{Ga}. (b) Antisites, N_{Ga} and Ga_N. (c) Octahedral interstitials, N_{Oct} and Ga_{Oct}. (d) Tetrahedral interstitials, N_{Tet} and Ga_{Tet}. (e) $\langle 2\bar{1}\bar{1}0\rangle$-oriented split interstitials formed with a host N atom, N^+-N$\langle 2\bar{1}\bar{1}0\rangle$ and Ga^+-N$\langle 2\bar{1}\bar{1}0\rangle$. (f) $\langle 2\bar{1}\bar{1}0\rangle$-oriented split interstitials formed with a host Ga atom, N^+-Ga$\langle 2\bar{1}\bar{1}0\rangle$ and Ga^+-Ga$\langle 2\bar{1}\bar{1}0\rangle$. (g) $\langle 01\bar{1}0\rangle$-oriented split interstitials formed with a host N atom, N^+-N$\langle 01\bar{1}0\rangle$ and Ga^+-N$\langle 01\bar{1}0\rangle$. (h) $\langle 01\bar{1}0\rangle$-oriented split interstitials formed with a host Ga atom, Ga^+-Ga$\langle 01\bar{1}0\rangle$ and N^+-Ga$\langle 01\bar{1}0\rangle$. The representations of atomic structures are the same as in Fig. 1. Large yellow balls in (c)-(h) label out the occupation sites for N/Ga atoms to form the N^+/Ga^+ interstitials. Arrows in (g) and (h) represent the exchange of N and Ga sites to form the opposite $\langle 01\bar{1}0\rangle$-oriented N-Ga dumbbells in the construction of Ga^+-N$\langle 01\bar{1}0\rangle$-o and N^+-Ga$\langle 01\bar{1}0\rangle$-o split interstitials, respectively.

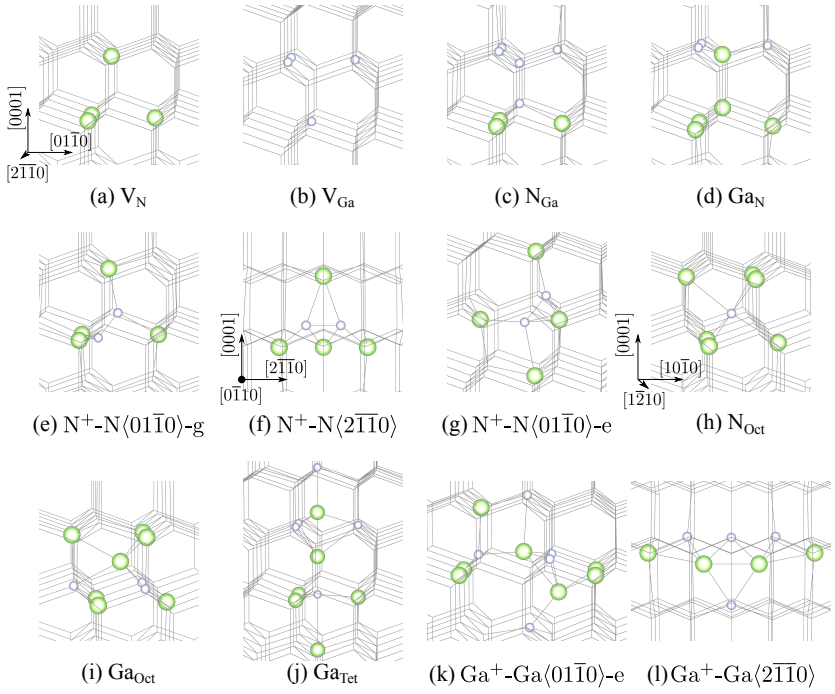

FIG. 6. (Color online) Perspective view of atomic structures of native point defects in wurtzite GaN relaxed by the SW potential. (a) V_N. (b) V_{Ga}. (c) N_{Ga}. (d) Ga_N. (e) N^+-N⟨01$\bar{1}$0⟩-g. (f) N^+-N⟨2$\bar{1}\bar{1}$0⟩. (g) N^+-N⟨01$\bar{1}$0⟩-e. (h) N_{Oct}. (i) Ga_{Oct}. (j) Ga_{Tet}. (k) Ga^+-Ga⟨01$\bar{1}$0⟩-e. (l) Ga^+-Ga⟨2$\bar{1}\bar{1}$0⟩. Small gray and large green balls represent the neighboring N and Ga atoms around the point defects, respectively. Other atoms and bonds in bulk GaN are simplified by the wire frames. The coordinate system illustrated in (a) is used by default, except the cases in (f) and (l) where the coordinate system is illustrated in (f), and the cases in (h) and (i) whose coordinate system is illustrated in (h).

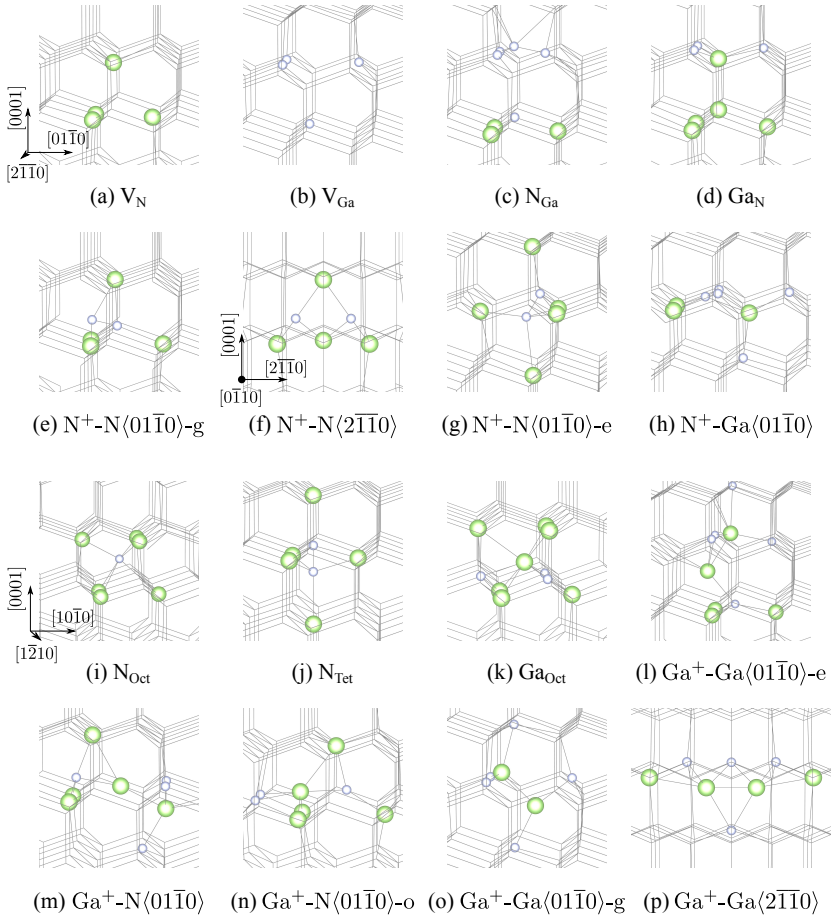

FIG. 7. (Color online) Perspective view of atomic structures of native point defects in wurtzite GaN relaxed by the MEAM potential. (a) V_N. (b) V_{Ga}. (c) N_{Ga}. (d) Ga_N. (e) N^+-N⟨01$\bar{1}$0⟩-g. (f) N^+-N⟨2$\bar{1}\bar{1}$0⟩. (g) N^+-N⟨01$\bar{1}$0⟩-e. (h) N^+-Ga⟨01$\bar{1}$0⟩. (i) N_{Oct}. (j) N_{Tet}. (k) Ga_{Oct}. (l) Ga^+-Ga⟨01$\bar{1}$0⟩-e. (m) Ga^+-N⟨01$\bar{1}$0⟩. (n) Ga^+-N⟨01$\bar{1}$0⟩-o. (o) Ga^+-Ga⟨01$\bar{1}$0⟩-g. (p) Ga^+-Ga⟨2$\bar{1}\bar{1}$0⟩. The representations of atomic structures are the same as in Fig. 6. The coordinate system illustrated in (a) is used by default, except the cases in (f) and (p) where the coordinate system is illustrated in (f), and the cases in (i) and (k) where the coordinate system is illustrated in (i).

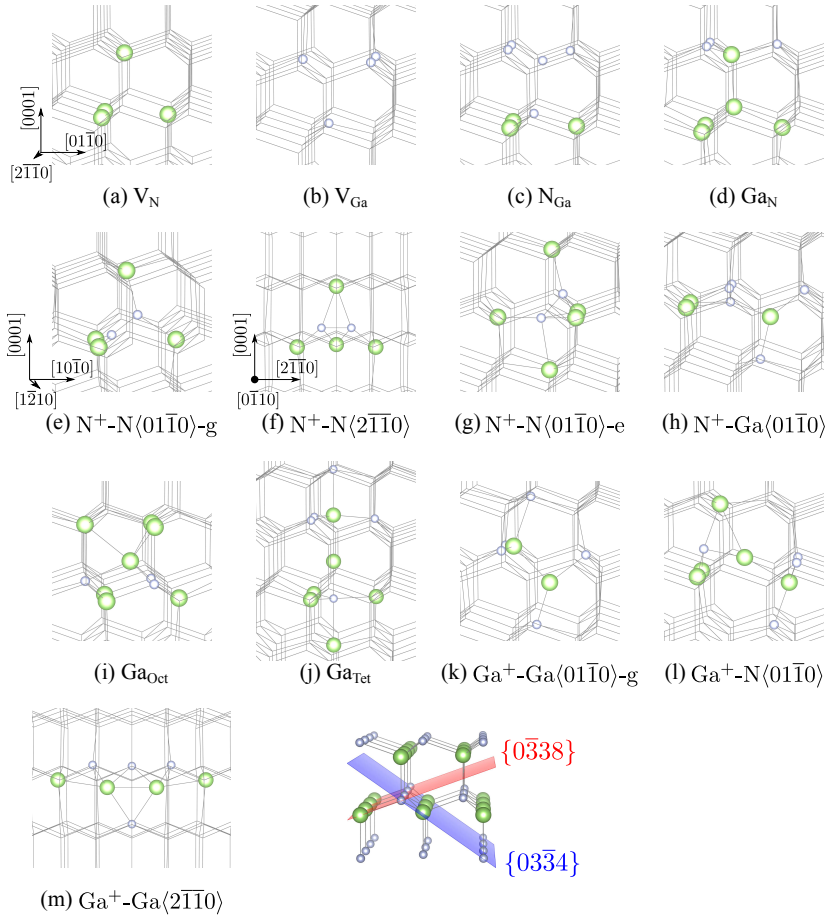

FIG. 8. (Color online) Perspective view of atomic structures of native point defects in wurtzite GaN relaxed by DFT calculations. (a) V_N. (b) V_{Ga}. (c) N_{Ga}. (d) Ga_N. (e) N^+-N⟨01$\bar{1}$0⟩-g. (f) N^+-N⟨2$\bar{1}\bar{1}$0⟩. (g) N^+-N⟨01$\bar{1}$0⟩-e. (h) N^+-Ga⟨01$\bar{1}$0⟩. (i) Ga_{Oct}. (j) Ga_{Tet}. (k) Ga^+-Ga⟨01$\bar{1}$0⟩-g. (l) Ga^+-N⟨01$\bar{1}$0⟩. (m) Ga^+-Ga⟨2$\bar{1}\bar{1}$0⟩. The representations of atomic structures are the same as in Fig. 6. The coordinate system illustrated in (a) is used by default, except the cases in (e) and (i) where the coordinate system is illustrated in (e), and the cases in (f) and (m) where the coordinate system is illustrated in (f). Inset indicates the {0$\bar{3}$38} plane (in red) where N-Ga pairs arrange in parallel, and the {03$\bar{3}$4} plane (in blue) where N-Ga pairs arrange in zigzag pattern.

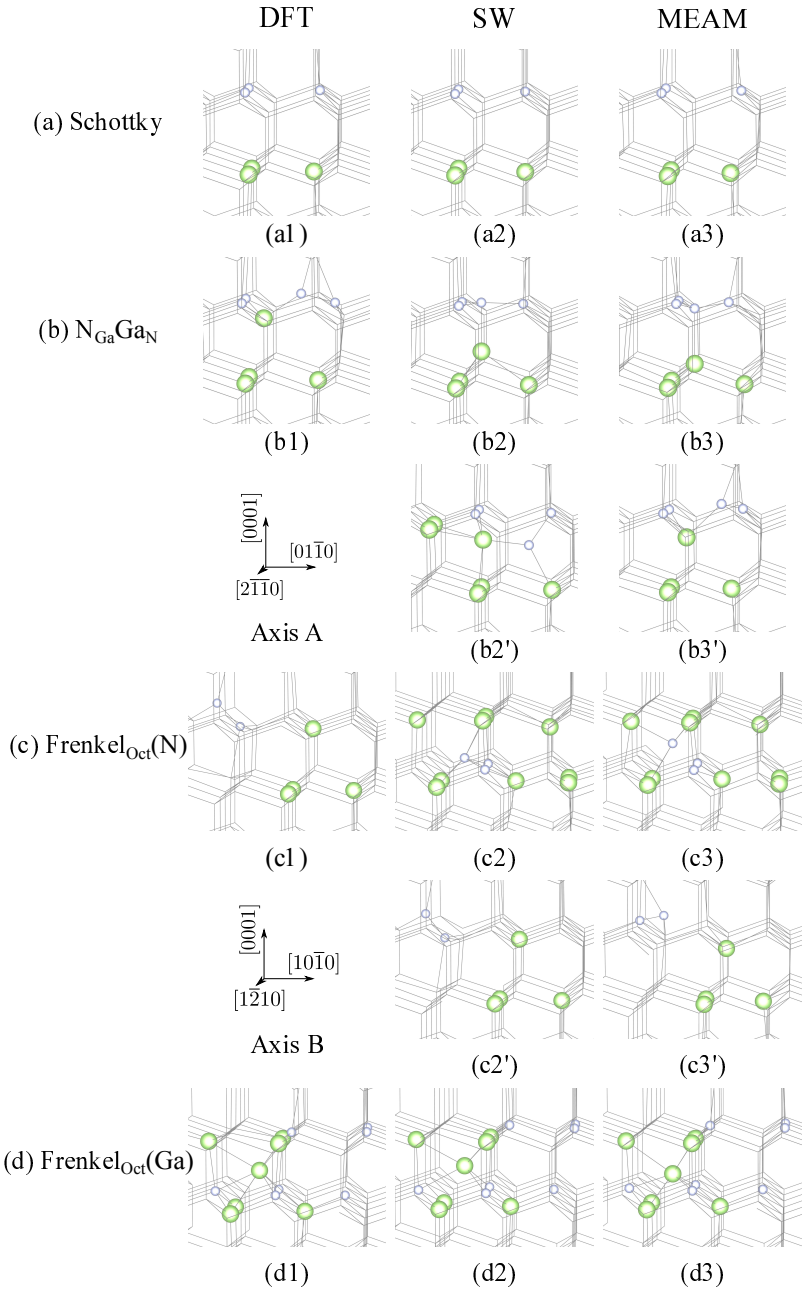

FIG. 9. (Color online) Perspective view of atomic structures of point defect complexes in wurtzite GaN relaxed by DFT (Left), SW (Middle) and MEAM (Right) potentials, respectively. (a) Schottky. (b) $N_{Ga}Ga_N$, where (b2') and (b3') are the relaxed structures by taking the DFT result in (b1) as the initial configuration. (c) $Frenkel_{Oct}$(N), where (c2') and (c3') are the relaxed structures by taking the DFT result in (c1) as the initial configuration. And (d) $Frenkel_{Oct}$(Ga). The representations of atomic structures are the same as in Fig. 6. The coordinate system denoted by 'Axis A' is used by default, except the cases in (c2), (c3), (d1), (d2) and (d3), which are coordinated by the axes denoted as 'Axis B'.

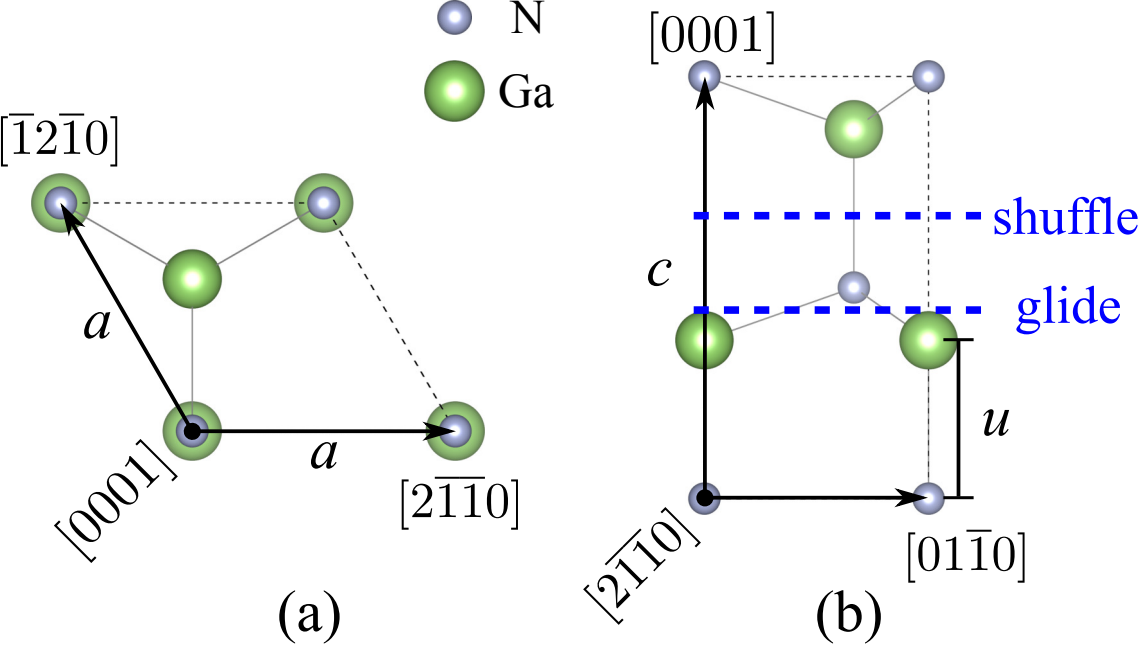
N
Ga
[$\bar{1}2\bar{1}0$]
a
a
[0001]
[$2\bar{1}\bar{1}0$]
(a)
[0001]
shuffle
c
glide
u
[$2\bar{1}\bar{1}0$]
[$01\bar{1}0$]
(b)

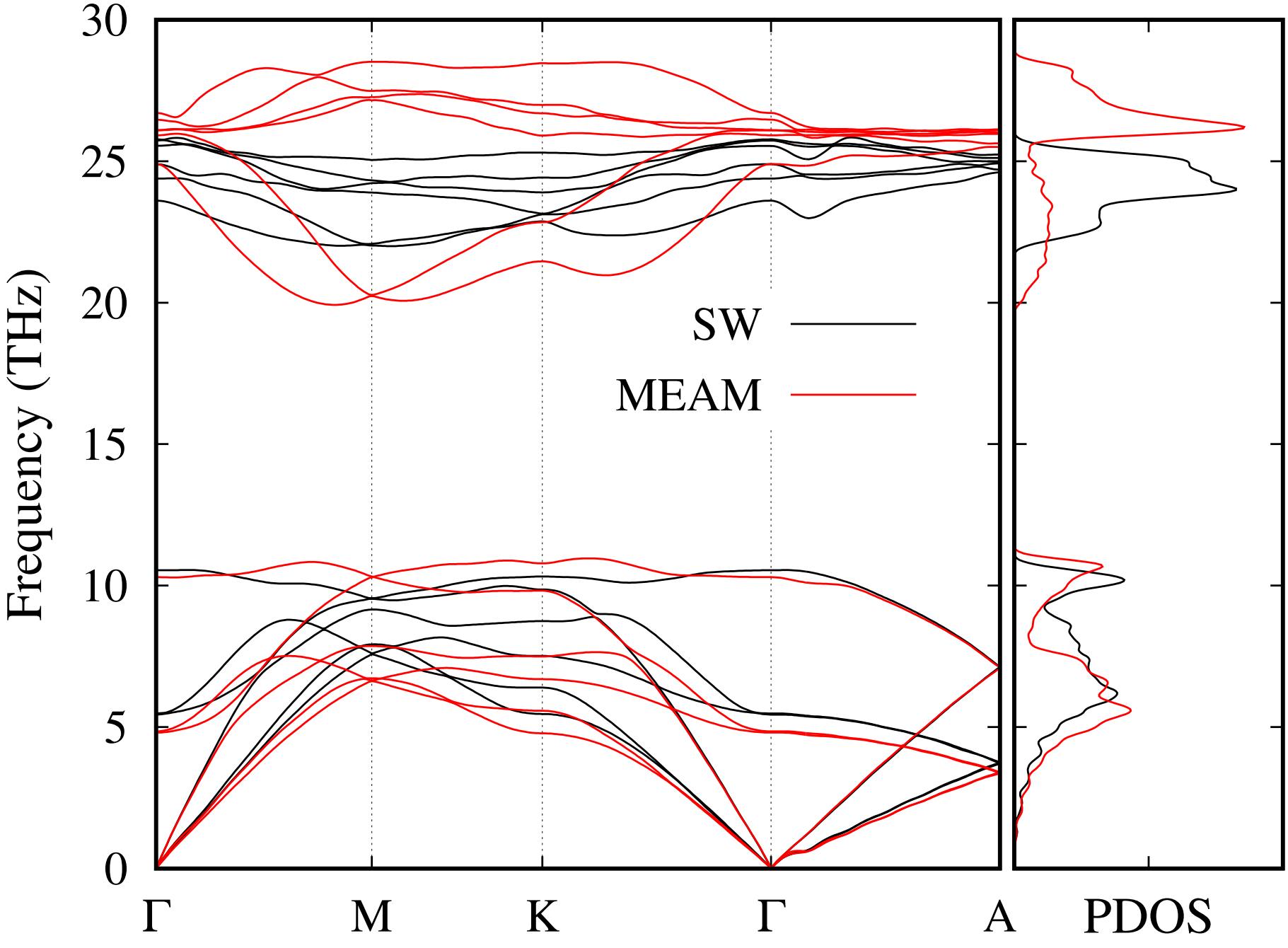
30
25
20
15
10
5
0
Frequency (THz)
SW
MEAM
Γ
M
K
Γ
A
PDOS

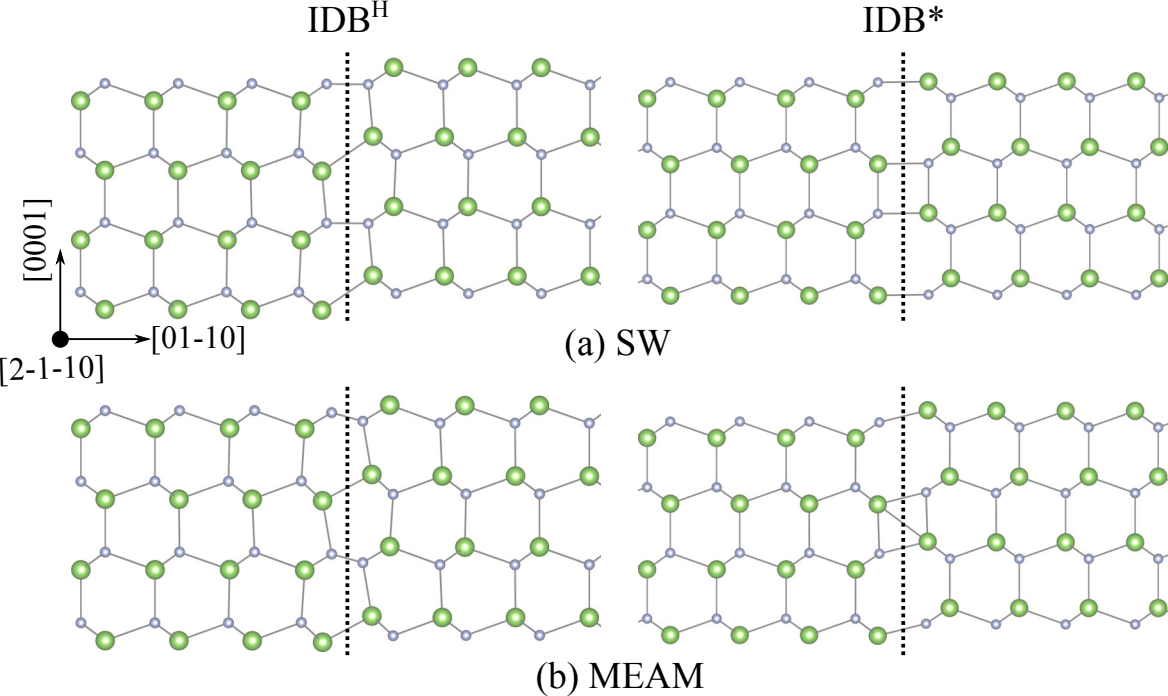
IDB^H
IDB*
[0001]
[01-10]
[2-1-10]
(a) SW
(b) MEAM

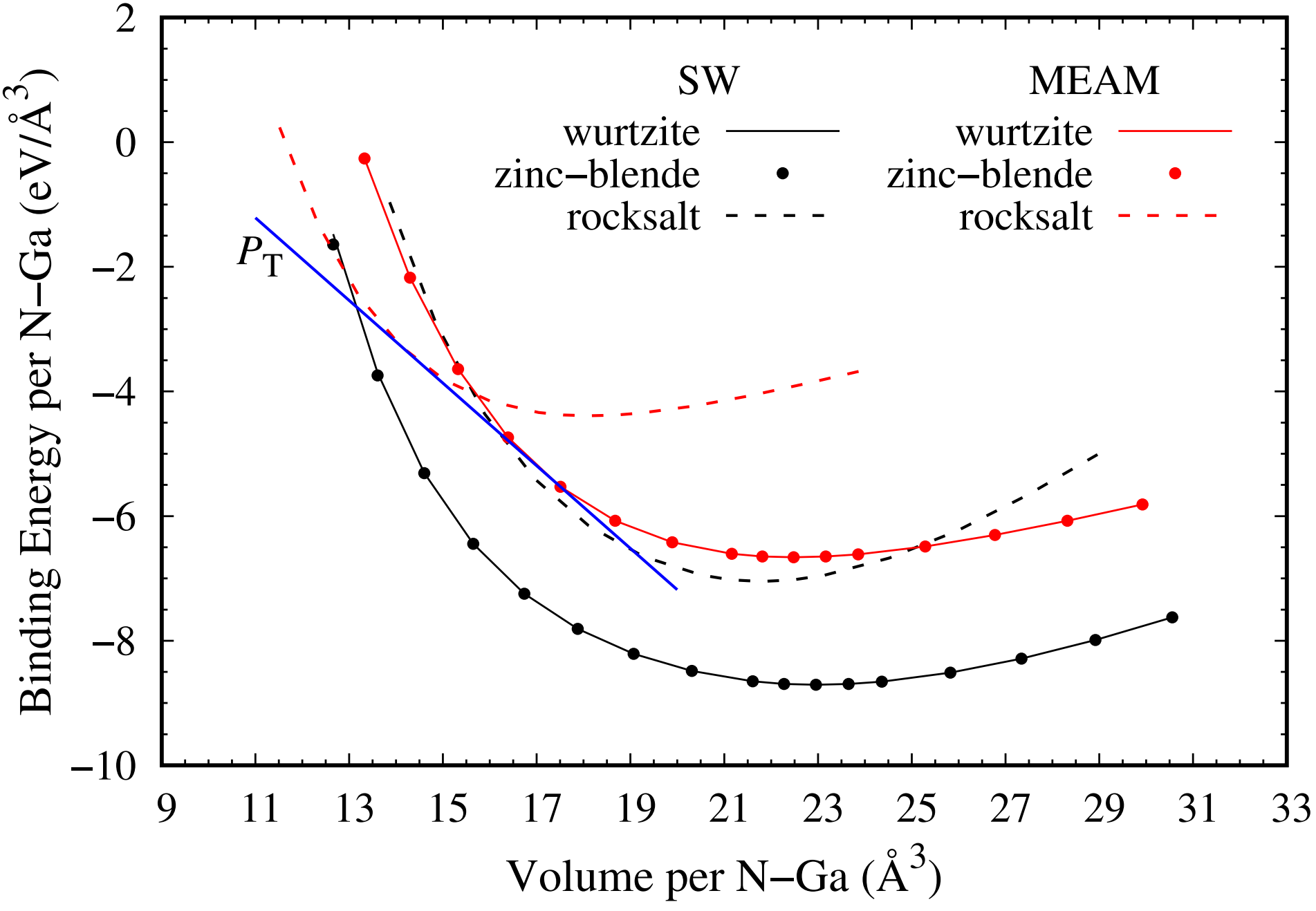
SW
wurtzite
zinc–blende
rocksalt
MEAM
wurtzite
zinc–blende
rocksalt
P_T
Binding Energy per N–Ga (eV/Å^3)
Volume per N–Ga (Å^3)
2
0
−2
−4
−6
−8
−10
9
11
13
15
17
19
21
23
25
27
29
31
33

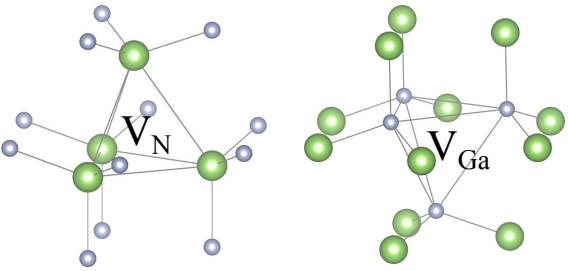

(a) Vacancies

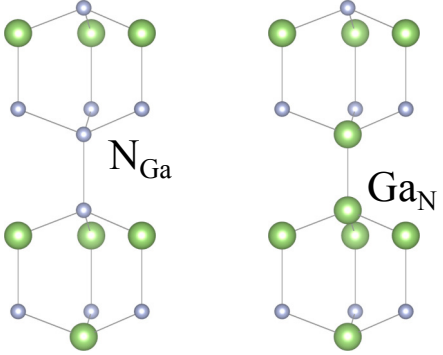

(b) Antisites

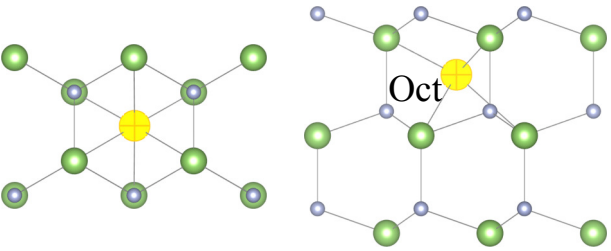

Plane view Side view

(c) Octahedral interstitials

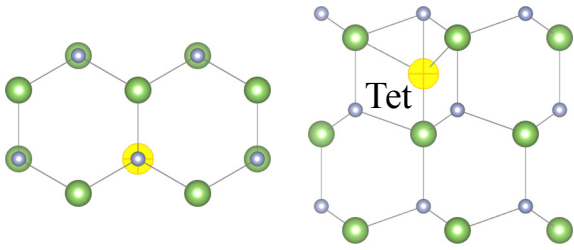

Plane view Side view

(d) Tetrahedral interstitials

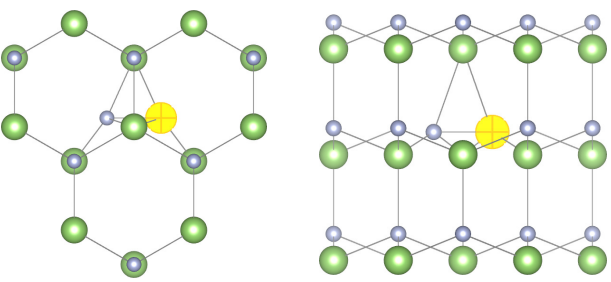

Plane view Side view

(e) N^+/Ga^+-N$\langle 2\bar{1}\bar{1}0\rangle$

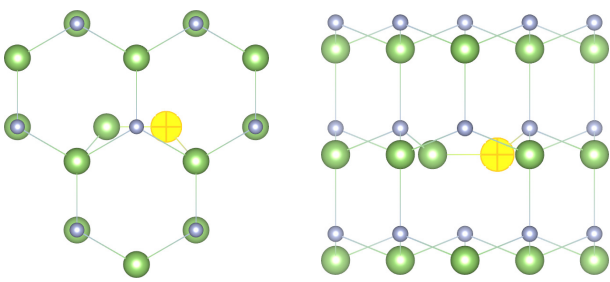

Plane view Side view

(f) N^+/Ga^+-Ga$\langle 2\bar{1}\bar{1}0\rangle$

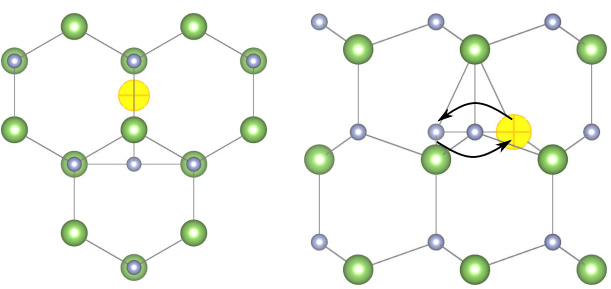

Plane view Side view

(g) N^+/Ga^+-N$\langle 01\bar{1}0\rangle$

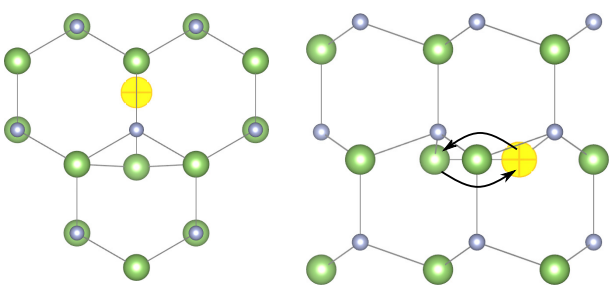

Plane view Side view

(h) N^+/Ga^+-Ga$\langle 01\bar{1}0\rangle$

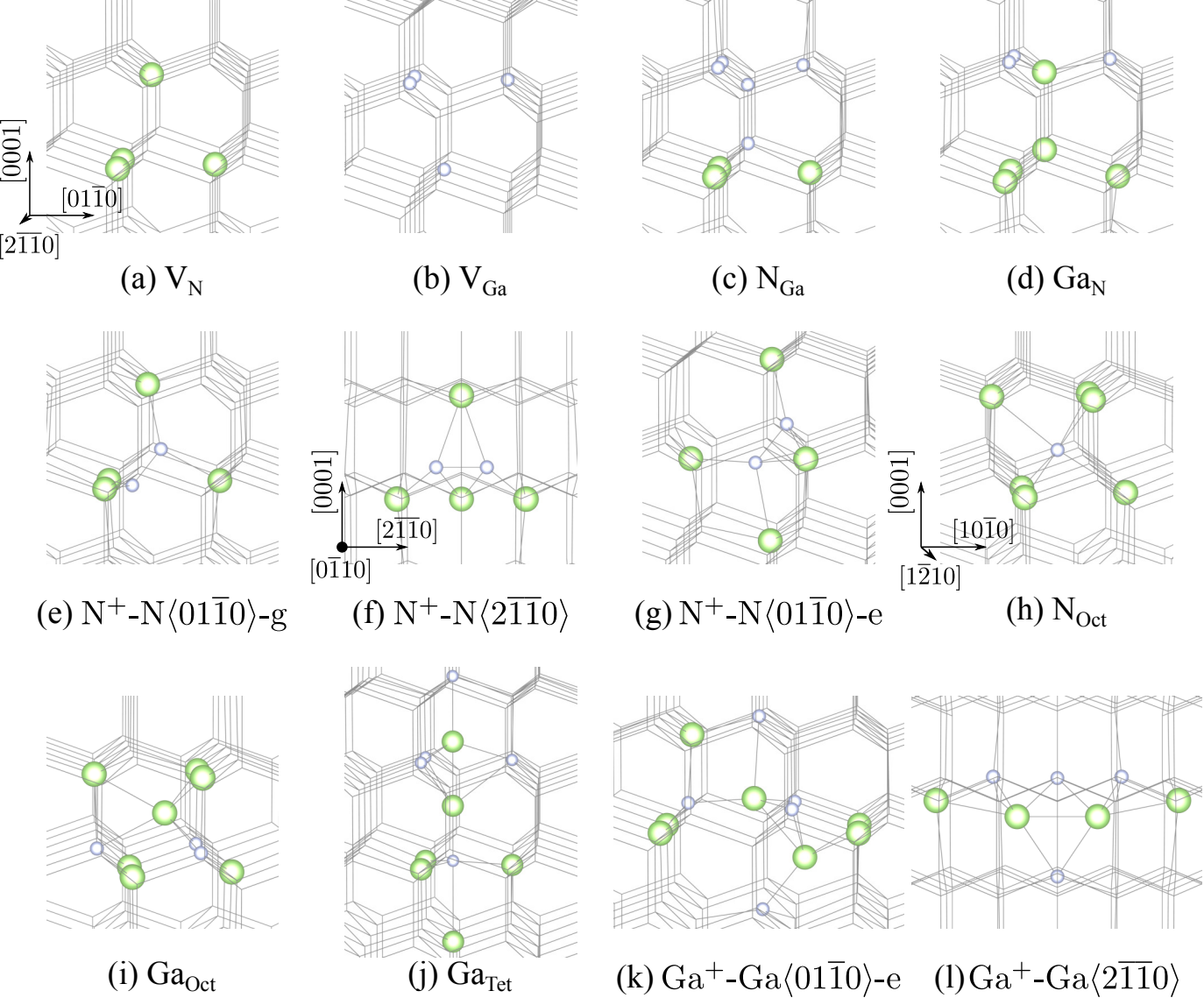

(a) V_N (b) V_{Ga} (c) N_{Ga} (d) Ga_N

(e) N^+-N$\langle 01\bar{1}0\rangle$-g (f) N^+-N$\langle 2\bar{1}\bar{1}0\rangle$ (g) N^+-N$\langle 01\bar{1}0\rangle$-e (h) N_{Oct}

(i) Ga_{Oct} (j) Ga_{Tet} (k) Ga^+-Ga$\langle 01\bar{1}0\rangle$-e (l) Ga^+-Ga$\langle 2\bar{1}\bar{1}0\rangle$

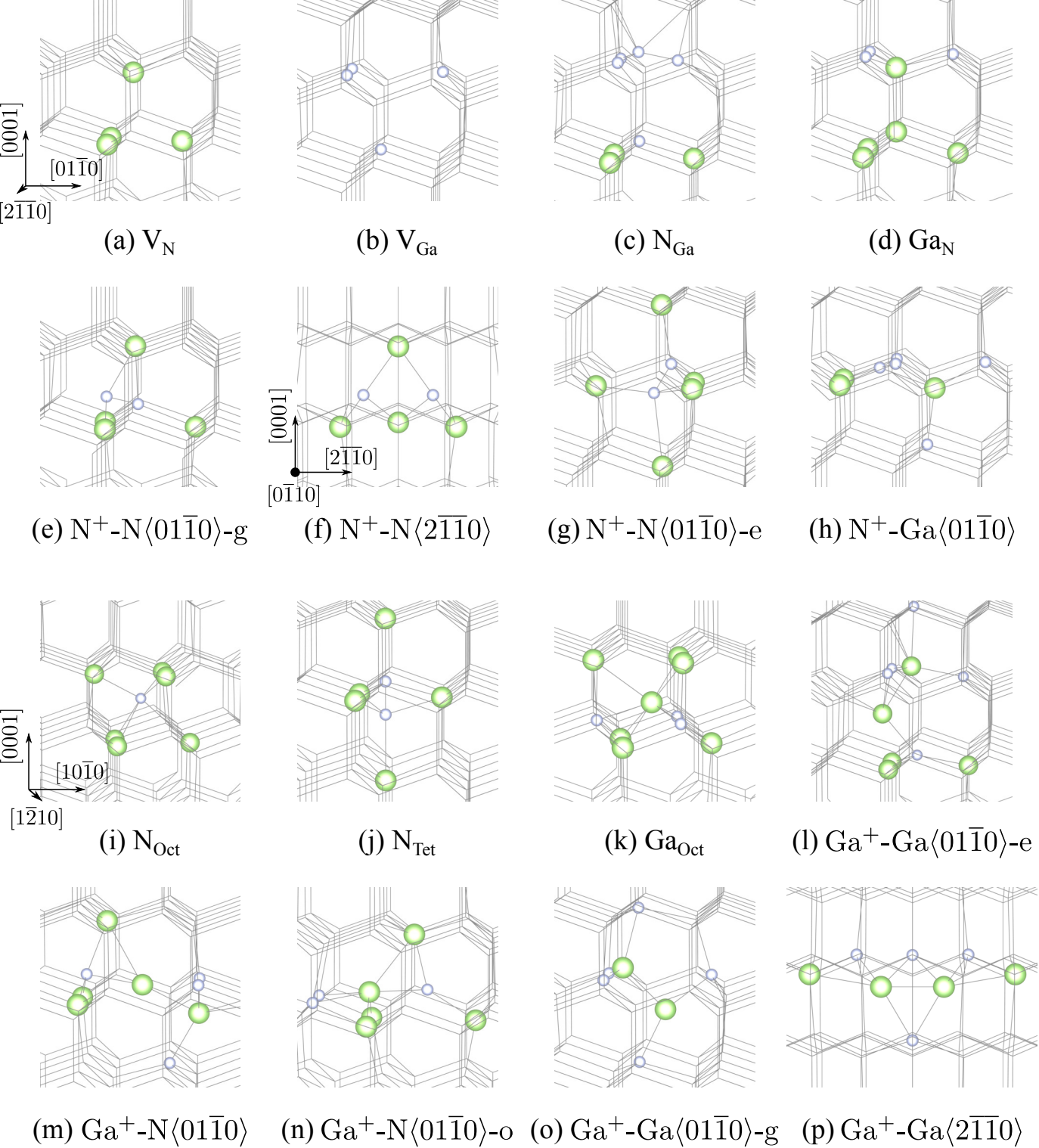
[0001]
[01$\bar{1}$0]
[2$\bar{1}\bar{1}$0]
(a) V_N
(b) V_{Ga}
(c) N_{Ga}
(d) Ga_N
(e) N^+-N⟨01$\bar{1}$0⟩-g
[0001]
[2$\bar{1}\bar{1}$0]
[0$\bar{1}$10]
(f) N^+-N⟨2$\bar{1}\bar{1}$0⟩
(g) N^+-N⟨01$\bar{1}$0⟩-e
(h) N^+-Ga⟨01$\bar{1}$0⟩
[0001]
[10$\bar{1}$0]
[1$\bar{2}$10]
(i) N_{Oct}
(j) N_{Tet}
(k) Ga_{Oct}
(l) Ga^+-Ga⟨01$\bar{1}$0⟩-e
(m) Ga^+-N⟨01$\bar{1}$0⟩
(n) Ga^+-N⟨01$\bar{1}$0⟩-o
(o) Ga^+-Ga⟨01$\bar{1}$0⟩-g
(p) Ga^+-Ga⟨2$\bar{1}\bar{1}$0⟩

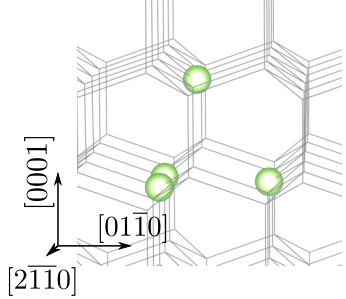

(a) V_N

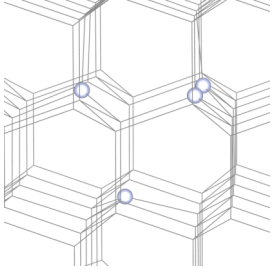

(b) V_{Ga}

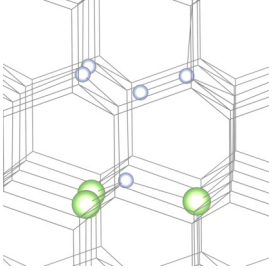

(c) N_{Ga}

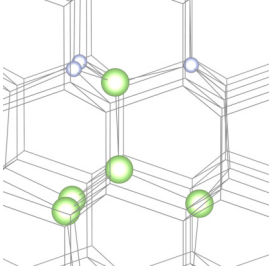

(d) Ga_N

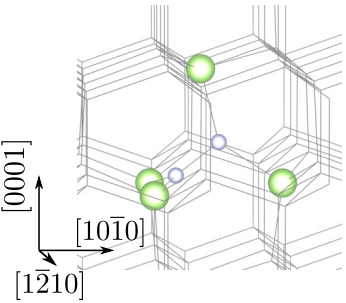

(e) N^+-N$\langle 01\bar{1}0\rangle$-g

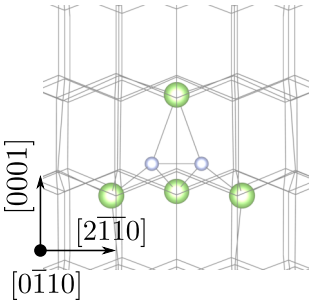

(f) N^+-N$\langle 2\bar{1}\bar{1}0\rangle$

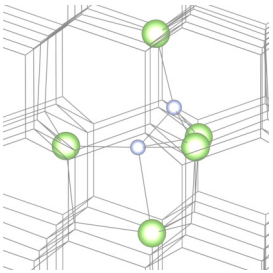

(g) N^+-N$\langle 01\bar{1}0\rangle$-e

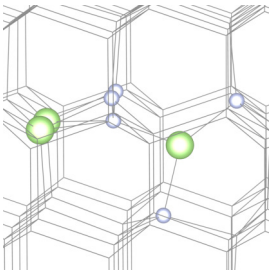

(h) N^+-Ga$\langle 01\bar{1}0\rangle$

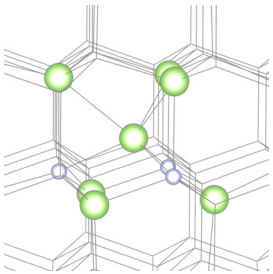

(i) Ga_{Oct}

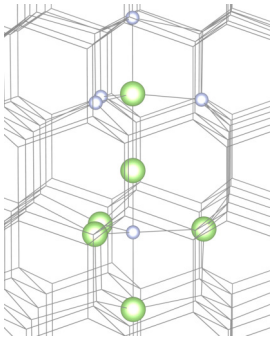

(j) Ga_{Tet}

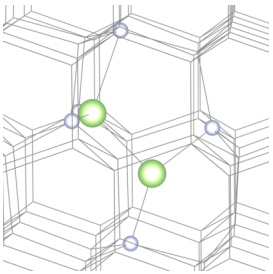

(k) Ga^+-Ga$\langle 01\bar{1}0\rangle$-g

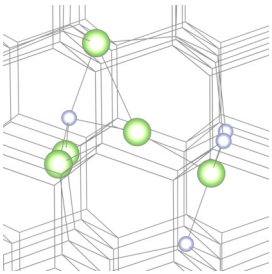

(l) Ga^+-N$\langle 01\bar{1}0\rangle$

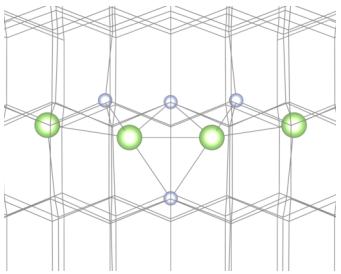

(m) Ga^+-Ga$\langle 2\bar{1}\bar{1}0\rangle$

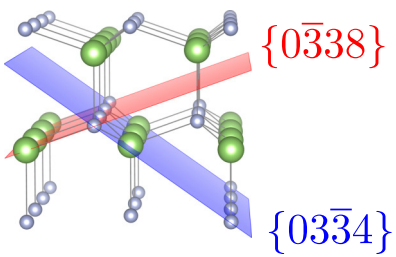

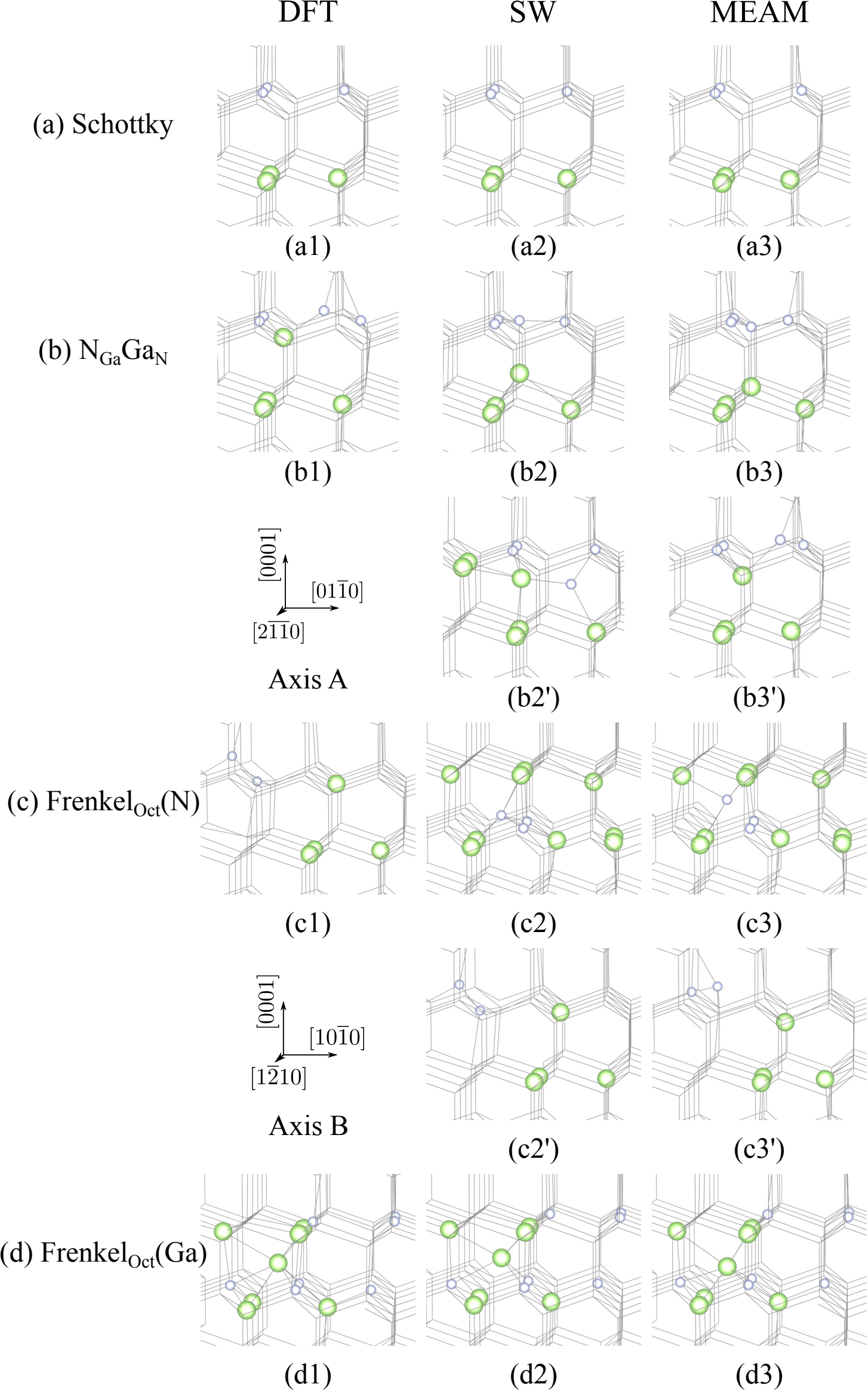
DFT
SW
MEAM
(a) Schottky
(a1)
(a2)
(a3)
(b) $N_{Ga}Ga_N$
(b1)
(b2)
(b3)
[0001]
[01$\bar{1}$0]
[2$\bar{1}\bar{1}$0]
Axis A
(b2')
(b3')
(c) $Frenkel_{Oct}(N)$
(c1)
(c2)
(c3)
[0001]
[10$\bar{1}$0]
[1$\bar{2}$10]
Axis B
(c2')
(c3')
(d) $Frenkel_{Oct}(Ga)$
(d1)
(d2)
(d3)